2012

Simulated Associating Polymer Networks

Joris Billen
Claremont Graduate University

Simulated Associating Polymer Networks

by

Joris Billen

A Dissertation
Submitted to the Faculty of
San Diego State University
and
Claremont Graduate University

In Partial Fulfillment of
the Requirements for the Degree of
Doctor of Philosophy
in
Computational Science

San Diego, California

Approved by:

Arlette R.C. Baljon

We, the undersigned, certify that we have read this dissertation by Joris Billen and approve it as adequate in scope and quality for the degree of Doctor of Philosophy.

Dissertation Committee:

Arlette R.C. Baljon, Chair

Andrew Cooksy, Member

Peter Salamon, Member

Allon Percus, Member

Adam Landsberg, Member

<div align="center">**Abstract of the Dissertation**</div>

<div align="center">Simulated Associating Polymer Networks</div>

<div align="center">by</div>

<div align="center">Joris Billen</div>

<div align="center">San Diego State University and Claremont Graduate University</div>

Telechelic associating polymer networks consist of polymer chains terminated by end-groups that have a different chemical composition than the polymer backbone. When dissolved in a solution, the endgroups cluster together to form aggregates. Their lifetime depends on temperature. At the micelle transition the temperature is sufficiently low for these aggregates to be substantial in size. At low temperature, a strongly connected reversible network is formed and the system behaves like a gel.

Telechelic networks are of interest since they are representative of biopolymer networks and are widely used in medical applications and consumer products. The material properties of these polymer networks pose complex and current problems in polymer physics. Many of the most basic questions concerning these networks, such as how they deform under stress, remain unanswered. Experiments under constant shear reveal a rich variety of non-Newtonian responses, including shear thinning and shear thickening. Within the shear thinning regime, shear banding is observed: when a constant shear is applied, the system forms two coexisting bands with different shear rates. The goal of this work is to study such systems using computer simulations. A hybrid molecular dynamics/Monte Carlo simulation is used for this purpose.

First we investigate how the network topology of an ensemble of telechelic polymers changes with temperature using graph theory. The aggregates are considered as nodes and the polymer chains as links between them. Our analysis shows that the degree distribution of the system is bimodal and consists of two Poissonian dis-

tributions with different average degrees. The number of nodes in each of them as well as the distribution of links depend on temperature. By comparing the eigenvalue spectra of the simulated gel networks with those of reconstructed networks, the most likely topology at each temperature is determined. Below the micelle transition the topology can be described by a robust bimodal network in which superpeer nodes are linked among themselves and all peer nodes are linked only to superpeers. At even lower temperatures the peers completely disappear leaving a structure of interconnected superpeers.

Many real life networks exhibit a spatial dependence, i.e. the probability to form a link between two nodes in the network depends on the distance between them. The study of the eigenvalue spectra of the simulated gel revealed that spatial dependent networks show universal spectral properties. This led to an in-depth study of such spectra. When increasing spatial dependence in Erdös-Rényi, scale-free and small-world networks, it is found that the spectrum changes. Due to the spatial dependence, the degree of clustering and the number of triangles increase. This results in a higher asymmetry (skewness). Our results show that the spectrum can be used to detect and quantify clustering and spatial dependence in a network.

Next, we study the rheological response of the polymer network under constant shear. The transient stress response shows an overshoot, followed by fluctuations around a lower, average value. When different shear rates are applied, there is a region in which the average stress does not increase significantly. Within this plateau, shear banding occurs. Experiments suggest possible differences between both bands in several properties. The simulation allows for a study of these differences on the microscopical scale. The average aggregate size is lower in the high shear rate band, due to an increase in aggregates consisting of a single endgroup. There is an increase in dynamics and this is highest in the high shear band. These changes are gradual

as a function of the distance between the moving walls, and we did not find a sharp increase at the interface. Next, we focus on structural changes of the sheared system as a whole, compared to the unsheared system. The aggregate size distribution becomes bimodal and preferential aggregate size formation decreases under shear. There is a decrease in links and a rearrangement of the structure under shear. This leads to larger aggregates that are connected by "stronger" links of high weight, consisting of multiple bridging chains. Such rearrangement is of importance in the observed decrease in stress in the transient stress response. The loop/bridge ratio increases, but only for high strain rates.

Finally we investigate the relation between percolation and gelation. Since the junctions between the endgroups in our system are temporary, geometric percolation does not occur at the gelation temperature. To explain the rheological changes that occur around this transition, only the network made up of endgroups that have junctions that survive over longer times is important. The percolation threshold, the time where the system shows 50% probability to percolate, increases with decreasing temperature. Vogel-Fulcher-Tamman (VFT) theory predicts that this time will diverge at $T = 0.29$. This is in agreement with the gelation temperature obtained from earlier measurements of relaxation times. A master curve can be constructed for percolation probability and survival rate by empirically shifting them up to $T = 0.6$. The scaling factors follow the Williams-Landel-Ferry (WLF) equations and the T_0 from WLF corresponds to the one from VFT. This is in support of recent ideas that gelation phenomena and glass transition show similarities.

Acknowledgements

In the first place, my acknowledgement goes out to Arlette Baljon, who has given me the opportunity to work under her skilled supervision. Her level of scientific guidance is superior and the longer I work on the project, the more I realize that this is a very subtile, high quality project that will certainly produce many results in the years to come. Being in "the field" now for several years and having witnessed advisors in all the "shapes" they come in, I came to realize that having an advisor like Arlette is a privilege that not many doctoral students get to experience. I have been always in a comfortable position, not having to worry about funding, getting high-quality scientific input, and experiencing very pleasant work circumstances.

Next, I want to thank the members of the committee, Adam Landsberg, Allon Percus, Andrew Cooksy, and Peter Salamon for always getting back to me quickly. It is an honor to have people with such impressive careers spending some of their valuable time on my work. Special thanks goes out to Avinoam Rabinovitch, for the guidance during the first two years and the many skype calls and email conversations afterwards. Also I was happy to work again with Rajesh Khare, who has been of great help in the last months of the work. Next, I must thank Mark Wilson for sharing his coding expertise with me and for having many good discussions and I wish him good luck with his own work. I also want to thank Jose Castillo, for running the program and the CSRC for providing me a tuition waiver. I acknowledge the financial support I got trough Prof. Baljon's NSF-grants. Also I thank the physics department for providing me additional TA-ships, which was a good experience. I thank the Inamori Foundation for my fellowship and providing me the opportunity to meet Dr. Kazuo Inamori.

I want to thank my mother for being understanding about my choice to be far

Contents

List of Figures

List of Tables

Chapter 1

Introduction

1.1   Associating polymer networks and gelation

Associating polymer networks consist of polymer chains terminated by endgroups with a different chemical composition. When dissolved in a solution, the endgroups can form junctions. Associating polymers in which the linking occurs through the endgroups are referred to as telechelic polymers. The term telechelic orginates from the Greek words *telos*, far, and *chelos*, claw, thus describing the molecule as having two claws far away from each other, i.e. at the extremities of the chain, able to grip something else. The great interest in telechelic polymers resides in the fact that such polymers can be used, generally together with suitable linking agents, to carry out three important operations: (1) chain extension of short chains to long ones by means of bifunctional linking agents, (2) formation of networks by use of multifunctional linking agents, and (3) formation of (poly)block copolymers by combination of telechelics with different backbones [4].

The behavior of the system depends on the rate at which junctions are formed [5, 6]. This rate is determined by the polymer (atomic) concentration and the temperature, as shown in figure 1.1. At low atomic concentration (high temperature) the
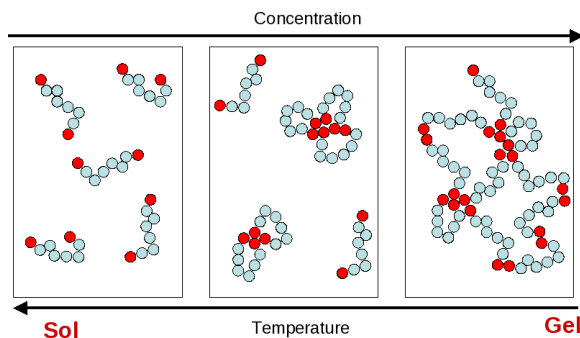
Figure 1.1: Transition from fluid, to mixture of micelles, to gelly state with decreasing temperature (increasing atomic concentration).

system is a sol; some polymers are dispersed in an abundant solution and the system behaves like a fluid. At higher polymer concentration (lower temperature) the likelihood of endgroups meeting each other increases and this leads to an increase in the number of connections between endgroups. The aggregation of endgroups leads to the formation of *micelles*, also referred to as *aggregates*. The corresponding transition is called the *micelle transition*. At even higher atomic concentration (low temperature) the formed micelles connect and a macroscopic network is formed. The solution now is structurally disordered as a liquid, but shows resistance to a stress as a solid. It is in a *gel state*, from "gelare", Latin for "to freeze". The crosslinks between the micelles are reversible: throughout time they break while new junctions are formed at different locations.

1.1.1 Chemical structure

Different chemical units may be used as linkers depending on the solvent, e.g., hydrophobic fragments on water-soluble polymers in aqueous solutions, and ionic groups on ionomers in organic solvents. An important group of associating polymers are hydrogels; hydrophilic polymers terminated by hydrophobic endgroups. Hydrogels are highly absorbent and can contain up to 99.9% water. Two such telechelic derivatives
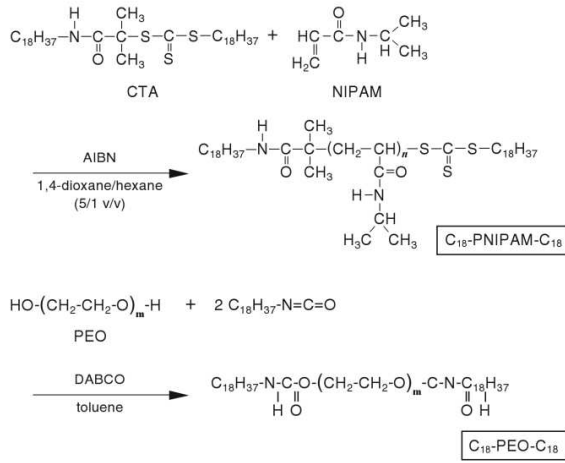
Figure 1.2: Preparation of telechelic hydrophobically modified poly(N-isopropyl-acrylamide), C_{18}-PNIPAM-C_{18} and telechelic hydrophobically modified poly (ethylene oxide), C_{18}-PEO-C_{18}. Taken from [1].

are hydrophobically modified poly(N-isopropylacrylamides) (HM-PNIPAM) and hydrophobically modified poly(ethylene oxide) (HM-PEO), which cary an octadecyl endgroup at each chain. The preparation method and chemical structure for these telechelics are shown in figure 1.2. Structurally the HM-PNIPAM samples bear close resemblance to the class of polymeric additives known as hydrophobic-ethylene oxide-urethene (HEUR) copolymers. HEUR is produced by chain extending poly(ethylene glycol) (PEG) with diisocyanate and both ends of the PEG chain are capped with hydrophobic moieties.

1.2 Rheological response

1.2.1 Definitions

When external forces are applied to a stationary object, stress and strain are the result. Stress is defined as the object's internal resisting forces, and strain is defined

3

as the displacement and deformation that occur. For a uniform distribution of internal resisting forces, stress can be calculated by dividing the force (F) applied by the unit area (A):

$$\text{Stress} = F/A. \tag{1.1}$$

Strain is defined as the amount of deformation per unit length (ΔL) of an object when a load is applied. Strain is calculated by dividing the total deformation of the original length by the original length (L):

$$\text{Strain} = \Delta L/L. \tag{1.2}$$

Experimental shear flow measurements are conducted in a Couette geometry, where the polymer solution is sandwiched between two concentric cylinders of which one is stationary, and the other rotating with velocity v (shown in figure 1.3). If the distance between the two cylinders is h, the shear rate $\dot{\gamma}$ is defined by:

$$\dot{\gamma} = \frac{v}{h}. \tag{1.3}$$

The viscosity η is a measure of how easily a material will flow when a stress is applied and is defined by:

$$\text{Stress} = \eta \cdot \dot{\gamma} \tag{1.4}$$

For a Newtonian liquid, the stress increases linear with the shear rate and the constant slope equals the viscosity. The simplest model for an elastic material is given by Hooke's law:

$$\text{Stress} = E \cdot \text{Strain} \tag{1.5}$$

where the strain is linearly proportional to the applied stress and E the elastic modulus. For a solid, which doesn't flow under stress, the viscosity is infinite. Viscoelastic materials show properties of both viscous as elastic materials, depending on the time
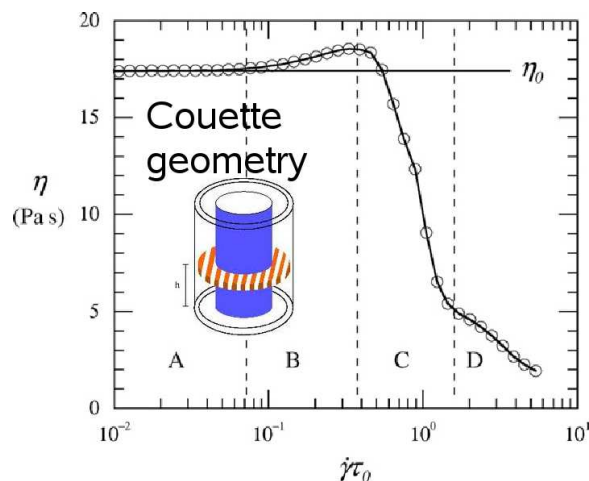
Figure 1.3: Viscosity versus imposed shear rate for a telechelic polymer, taken from [2].

scale. If a stress is applied over a short time scale, the material relaxes back to its initial shape after the stress is stopped. If stress is applied over a longer time scale, the material will flow. Finally the relaxation time τ_0, is a characteristic time scale that describes how a polymer chain returns to equilibrium after a stress is applied.

1.2.2 Shear thinning and thickening

Associating polymers are viscoelastic materials that are of often studied because of their rheological behavior. An example is shown in figure 1.3 for a PEO-based telechelic polymer [2].

At low shear rates, solutions of associative polymers show Newtonian behavior (regime A). When the reciprocal shear rate is of the order of the relaxation time or beyond, a rich variety of non-Newtonian responses is found. At moderate shear rates (regime B), shear thickening is observed, the viscosity increases with shear rate. This is attributed to stretching of the polymer chains (bridges) due to the applied flow. At higher shear rates the materials are deformed at rates faster than they can

5

structurally adapt and part of the structure in the quiescent state is broken down .
This leads to a decrease of the viscosity with shear rate (shear thinning, regime C).
Shear thinning can make the flow inhomogeneous, leading to the formation of two or
more bands of differing shear rate - a phenomena called shear banding. In regime D,
even though still shear thinning, the flow becomes homogeneous again.

1.2.3   Wormlike micelles and telechelic polymers

We note that a network-forming system closely related to telechelics are wormlike
micelles (WMs): entangled solutions of long and flexible surfactant cylinders [7]. A
surfactant reduces the surface tension of the system in which it is dissolved. The ba-
sic surfactant molecule is amphiphilic, meaning it possesses both hydrophilic (water-
loving) and hydrophobic, or lyophilic (oil-loving), groups that are chemically bonded
together. When placed in water, and at a high enough atomic concentration, sur-
factant molecules will arrange themselves together such that the tails become closely
packed together in order to minimize their contact with water. This self-assembling
process results in the formation of aggregates of surfactant molecules in solution.
Based on several factors the micelle can take a specific form such as a cylinder. This
can grow into a long wormlike micelle with increasing surfactant concentration. A
WM is only held together by relatively weak physical attractions/repulsions which
break and reform with time. Both telechelics and WMs show the ability to form highly
viscous solutions with relatively simple viscoelastic behavior. Throughout chapter 5,
which discusses the rheological response of the simulated gel network, we will often
refer to WMs.

1.3 Motivation for the research and technology assessment

Associating polymers are representative for several biopolymers. The study of biopolymer networks and gels lies at the heart of the understanding of the mechanical properties of the cytoplasm. The mechanical rigidity of the intracellular material is largely governed by the cytoskeleton, a complex network of filamentous proteins, cross-links, and other associated proteins. A key player in this cytoskeleton is F-actin, which exhibits significant rigidity on the cellular scale. The actin cortex is a polymeric gel that provides mechanical stability and plays a key roll in cell motion [8]. Development of models that describe the stress response of associating polymer networks, can be applied to the behavior of biologically important macromolecules such as DNA and actin [9].

Polymer gels are important for medical applications. Fibrin gels, responsible for blood clothing, are studied for tissue engineering purposes and the production of synthetic scaffolds [10]. Biocompatibility is an essential requirement for medical gels, and therefore gelatin, which is derived from the natural matrix protein collagen (the main protein in connective tissue and present in muscles), is ideally suited [11]. Kilotons of gelatin with a billion dollar market value is used on annual basis. Novel gelatin materials are being developed for bone, retinal, and other implants in vascular protheses, sponge embolization therapy, medical glues, blood supplementation fluids, and vaccines. The animal origin of gelatin poses risk of contamination and immune responses. Therefore gelatin-like polymers with a general design, offering independent tuning of the cross-link density, melting temperature, and biocompatibility of the gel, are designed. Hydrogels are found in laxatives, skin creams, medical electrodes, breast implants and dressings for healing of burn wounds. They show potential for controlled

release drug delivery. The gel can be implemented in living tissue (such as the brain) and carry a drug that gets exposed to the diseased cells [12]. Hydrogels have also been investigated as cartilage replacement materials due to the high water content potentially leading to low friction, low wear, and rubbery or pliable nature similar to native cartilage [13]. The moduli can be in the range of native tissues to match the mechanical properties of the polymer matrix of those of the surrounding tissue. PEO-based triblock copolymer hydrogels are created with a desired elastic modulus [14]. For other applications, gels with huge elastic moduli over 10kPa can be created. Injectable hydrogels recently drew media attention as they were shown to be able to repair tissue damaged by a heart attack [15]. Hydrogels that are responsive to specific molecules, such as glucose and antigens, can be used in biosensors [16].

Associating polymers are found in a wide variety of consumer products. Among all the associative polymers, HEUR offers the best balance of application rheology and dry film performance. They are usually added either to modify the rheology of aqueous solutions or to increase the stability of dispersions. HEUR polymers are being used in paint formulation, paper coating, and shampoo. Also hydrogels are very common in products such as contact lenses, diapers, paintball fill, printheads, spandex, foam cushions, and thickener in foods, paint and adhesives. Associating polymers have potential for self-healing materials. Due to the constant formation of new junctions, fractures can be created and healed reversibly [17]. NASA is interested in such materials for construction of self-healing aircrafts and gas tanks that are like biological organisms, having the ability to sense damage in their conditions and essentially heal themselves. Another possible application is as a coating layer for cars that repairs itself when scratched. For many polymer materials the reliability and endurance is still limited. It is believed that better understanding of flow during processing can be used to increase robustness.

1.4 Outline of the dissertation

The dissertation is organized as follows. Chapter 2 explains the simulation details of the model used to describe the polymer network. In chapter 3 we apply graph theory to study the changes in topology that accompany the micelle and gel transitions. Therein a study of the eigenvalue spectrum of the network is performed. In chapter 4 we focus on explaining the universal properties of the eigenvalue spectra for spatial dependent networks, that were encountered during the previous chapter. Chapter 5 treats shear-induced effects with a strong emphasis on shear banding. Finally, chapter 6 discusses the relation between the gel transition and percolation.

Chapter 2

Model and methods

The model used for simulating telechelic polymers is a hybrid model consisting of a Molecular Dynamics Simulation (MDS) with a Monte Carlo (MC) step. To model the beads on one polymer chain, we make use of the standard bead-spring model by Kremer and Grest [18]. To describe the interaction between endgroups this model has been tailored by Baljon [19] to include the possibility for the endgroups to connect. These connections and hence the network structure are constantly changing; breaking and formation of the junctions between endgroups is determined by a stochastic process through the MC step. The model continuously gathers information on both the position of the monomers in the system and on the network structure, by keeping track of what endgroups are connected to each other.

2.1   Molecular dynamics simulation

Each monomer moves according to the equations of motion:

$$\ddot{m}\vec{r}_i = \vec{\bigtriangledown} U_i\left(\vec{r}_i\right) - \Gamma \vec{r}_i + \vec{W}_i\left(t\right) \tag{2.1}$$

with U_i the total interaction potential on particle i, which will be extensively discussed in the next section. Γ is a friction constant and W_i a Gaussian white source that determines the temperature of the system. By integrating the equations of motion

we can calculate the position at timestep $t + \delta t$. Thereto a fifth order Gear predictor-corrector algorithm is used with $\delta t = 0.005\tau$, where the choice of δt is inspired by [18]. It consists of three essential steps [20]:

- Predictor. From the positions and their time derivatives up to the 5th order, all known at time t, the same quantities are predicted at time $t + \delta t$ by means of a Taylor expansion. Suppose $v(t) = \frac{dr(t)}{dt}$ is the velocity of the particle, $a(t) = \frac{d^2r(t)}{dt^2}$ the acceleration, $b(t) = \frac{d^3r(t)}{dt^3}$, $c(t) = \frac{d^4r(t)}{dt^4}$, $d(t) = \frac{d^5r(t)}{dt^5}$, and $e(t) = \frac{d^6r(t)}{dt^6}$, then:

$$r^p(t + \delta t) = r(t) + \delta t v(t) + \frac{1}{2}\delta t^2 a(t) + \frac{1}{6}\delta t^3 b(t) + \frac{1}{24}\delta t^4 c(t) + \frac{1}{120}\delta t^5 d(t) + \frac{1}{720}\delta t^6 e(t) \tag{2.2}$$

$$v^p(t + \delta t) = v(t) + \delta t a(t) + \frac{1}{2}\delta t^2 b(t) + \frac{1}{6}\delta t^3 c(t) + \frac{1}{24}\delta t^4 d(t) + \frac{1}{120}\delta t^5 e(t) \tag{2.3}$$

$$a^p(t + \delta t) = a(t) + \delta t b(t) + \frac{1}{2}\delta t^2 c(t) + \frac{1}{6}\delta t^3 d(t) + \frac{1}{24}\delta t^4 e(t) \tag{2.4}$$

$$b^p(t + \delta t) = b(t) + \delta t c(t) + \frac{1}{2}\delta t^2 d(t) + \frac{1}{6}\delta t^3 e(t) \tag{2.5}$$

$$c^p(t + \delta t) = c(t) + \delta t d(t) + \frac{1}{2}\delta t^2 e(t) \tag{2.6}$$

$$d^p(t + \delta t) = d(t) + \delta t e(t) \tag{2.7}$$

- Force evaluation. Using equation 2.1 and the predicted new position $r^p(t + \delta t)$, the acceleration $a^c(t + \delta t)$ can now be calculated. The result will be in general different from the predicted acceleration. The difference between the two constitutes an error signal:

$$\Delta a(t + \delta t) = a^p(t + \delta t) - a^c(t + \delta t) \tag{2.8}$$

- Corrector. This error signal is used to correct positions and their derivatives.

11

All the corrections are proportional to the error signal:

$$r^c(t + \delta t) = r^p(t + \delta t) + \alpha_0 \Delta a(t + \delta t) \tag{2.9}$$

$$v^c(t + \delta t) = v^p(t + \delta t) + \alpha_1 \Delta a(t + \delta t) \tag{2.10}$$

$$a^c(t + \delta t) = a^p(t + \delta t) + \alpha_2 \Delta a(t + \delta t) \tag{2.11}$$

$$b^c(t + \delta t) = b^p(t + \delta t) + \alpha_3 \Delta a(t + \delta t) \tag{2.12}$$

$$c^c(t + \delta t) = c^p(t + \delta t) + \alpha_4 \Delta a(t + \delta t) \tag{2.13}$$

$$d^c(t + \delta t) = d^p(t + \delta t) + \alpha_5 \Delta a(t + \delta t) \tag{2.14}$$

with $\alpha_0 = 3/16$, $\alpha_1 = 251/360$, $\alpha_2 = 1$, $\alpha_3 = 11/18$, $\alpha_4 = 1/6$, $\alpha_5 = 1/60$.

The results of the MDS will be determined by the different potentials that are at play between the atoms. These are described in the next section.

2.2 Interaction potentials

2.2.1 Bead-spring model

Any two particles i and j in the system experience a Lennard-Jones potential:

$$U^{lj}(r_{ij}) = 4\epsilon \left[\left(\frac{\sigma}{r_{ij}} \right)^{12} - \left(\frac{\sigma}{r_{ij}} \right)^6 - \left(\frac{\sigma}{r_c} \right)^{12} + \left(\frac{\sigma}{r_c} \right)^6 \right], r_{ij} < r_c = 2^{1/6}. \tag{2.15}$$

In the simulation all particles have a diameter of 1 σ and a mass m (coarse-grained), even though chemically there are obviously large distinctions between endgroups and chain monomers. The unit of time is $\tau = \sigma(m/\epsilon)^{1/2}$ where ϵ is the unit of energy. Also temperature is expressed in ϵ, although by convention this will not be mentioned explicitly. Throughout the simulation $k_B = 1$ is used.

The Lennard-Jones potential is shown in figure 2.1 (dashed line) and is purely repulsive: it is truncated by setting $U^{lj}(r_{ij}) = 0$ for $r_{ij} > r_c$. Therefore all beads will repel each other (excluded volume interactions). Also it is shifted by 0.25 ϵ such that
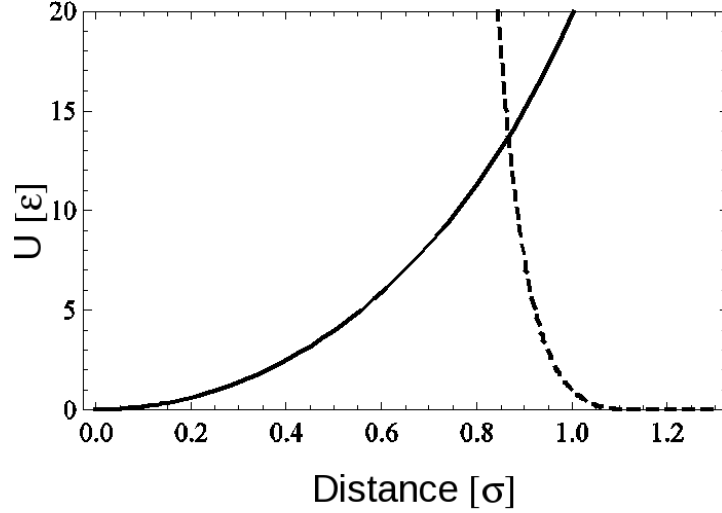
Figure 2.1: Fene potential (solid line) and Lennard-Jones potential (dashed).

$U^{lj}(r_c) = 0$.

Neighboring beads on a chain experience, in addition to the Lennard Jones potential, a finite nonlinear elastic potential (fene) that is defined as:

$$U^{fene}(r_{ij}) = -\frac{1}{2}kR_0^2 \ln\left[1 - \left(\frac{r_{ij}}{R_0^2}\right)^2\right], r_{ij} < R_0 = 1.5\sigma \qquad (2.16)$$

and infinite otherwise. The fene is shown in figure 2.1 (solid line). The effect of this potential is to connect the beads on a chain with springs. $\kappa = 30\epsilon\sigma^{-2}$ is a measure for the strength of the springs and R_0 sets the maximum bond length. They have been adjusted so bonds can not cross or break. The average length of a bond between neighboring beads on a chain is 0.97σ, corresponding to the minimum of $U^{lj}(r_{ij}) + U^{fene}(r_{ij})$.

The technique described in this subsection is the traditional bead-spring model for polymer chains. For telechelic polymers now this needs to be extended by including the possibility of junctions between the chain endgroups.

13
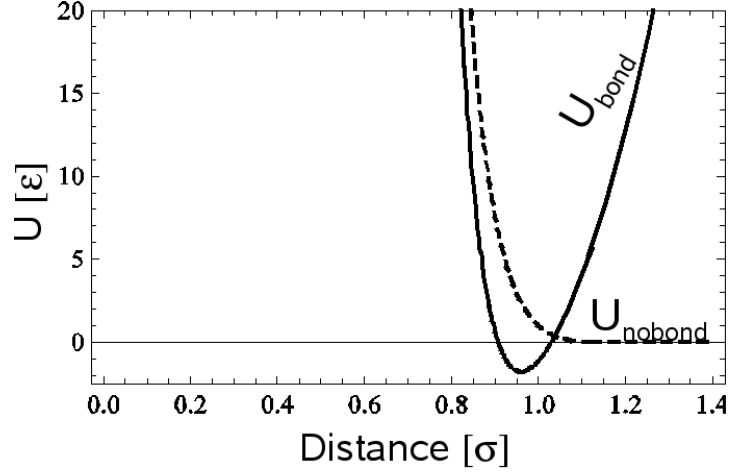
Figure 2.2: The interaction energy between two endgroups that have formed a junction (solid line) or that have not formed a junction (dashed).

2.2.2 Endgroups

A junction between two endgroups is modeled using the fene potential from equation (2.16). Upon formation of a junction both endgroups also experience a large negative association energy:

$$U^{assoc} = -22\epsilon \qquad (2.17)$$

that lowers the overall energy of the endgroups by a large constant and is necessary for keeping the bond from breaking right away, making the bonded state more reversible. Therefore if two endgroups have formed a bond, the total energy of the junction is:

$$U^{bond}(r_{ij}) = U^{fene}(r_{ij}) + U^{lj}(r_{ij}) + U^{assoc}(r_{ij}) \qquad (2.18)$$

while if there is no bond between them, their energy is

$$U^{nobond}(r_{ij}) = U^{lj}(r_{ij}). \qquad (2.19)$$

Both possibilities are shown in figure 2.2.

14

particles	Total interaction potential
any monomer pair	$U^{lj}(r_{ij})$
neighboring beads on a chain	$U^{lj}(r_{ij}) + U^{fene}(r_{ij})$
two endgroups with junction	$U^{lj}(r_{ij}) + U^{fene}(r_{ij}) + U^{assoc}$
two endgroups no junction	$U^{lj}(r_{ij})$
endgroup attached to the wall	$U^{lj}(r_{ij}) + U^{fene}(r_{ij})$

Table 2.1: Overview of potentials used in the simulation.

2.2.3 The wall

In the z-direction the system is confined by two walls, each consisting of 800 beads spread over two layers in FCC structure. The 1600 wall atoms have a radius of 0.8σ and are all connected to a lattice site by a harmonic potential with spring constant $260\epsilon\sigma^{-2}$. The number of grafted chains should be low, so it does significantly influence the aggregate size distribution, but high enough to transfer the applied shear to the gel system. Therefore 5% of the endgroups are permanently attached to the wall: 50 to the top wall and 50 to the bottom wall. They form a junction with a wall atom using U^{fene} that will never be broken. These grafted chains are spread over the surface in a square lattice, the lattice on the top wall is shifted in such a way that each lattice point corresponds to the middle of a unit cell on the lower wall.

The current section described the static properties of the system. As a summary an overview is given for all the possible interaction potentials in table 2.1. The next section describes how to take into account the continuous formation and breaking of the junctions.

2.3 Dynamics of junctions between endgroups: Monte Carlo

Every 0.1τ an attempt is made to destroy all the existing junctions and create new ones using a Monte Carlo step. The probability of success depends on the energy difference between the possible new state and the old state $\Delta U(r_{ij})$:

$$P(r_{ij}) \sim \exp\left(-\frac{\Delta U(r_{ij})}{k_B T}\right). \tag{2.20}$$

with ΔU depending on the situation defined as:

$$\Delta U_{form}(r_{ij}) = U^{bond} - U^{nobond} = U^{assoc}(r_{ij}) + U^{fene}(r_{ij}) \tag{2.21}$$

$$\Delta U_{break}(r_{ij}) = U^{nobond} - U^{bond} = -\left(U^{assoc}(r_{ij}) + U^{fene}(r_{ij})\right) \tag{2.22}$$

These quantities are shown in figure 2.3. In both situations $\Delta U(r_{ij}) = 0$ for $r_{\Delta U_0} = 1.038\sigma$. When the potential new state is at an energy level that is lower than the current state, the attempt will always occur. Therefore for the formation of a bond equation (2.20) yields a probability of 1 for $r_{ij} \leq r_{\Delta U_0}$, and a chance between 0 and 1 depending on $\Delta U / k_B T$ otherwise. For breaking a junction the probability is 1 for $r_{ij} \geq r_{\Delta U_0}$ and between 0 and 1 otherwise. This shows that a bond between 2 endgroups that is only stretched for 0.068 σ further than the average bond length will already break with a probability of 1, showing the stiffness of the spring potential from equation (2.16).

2.4 System size

The system consists of 1000 polymer chains of 8 beads long hence there are 8000 monomers of which 2000 are endgroups. The boxsize is 23.69 σ in the x-direction, 20.52 σ in the y-direction and 27.84 σ in the z-direction. There are periodic boundary
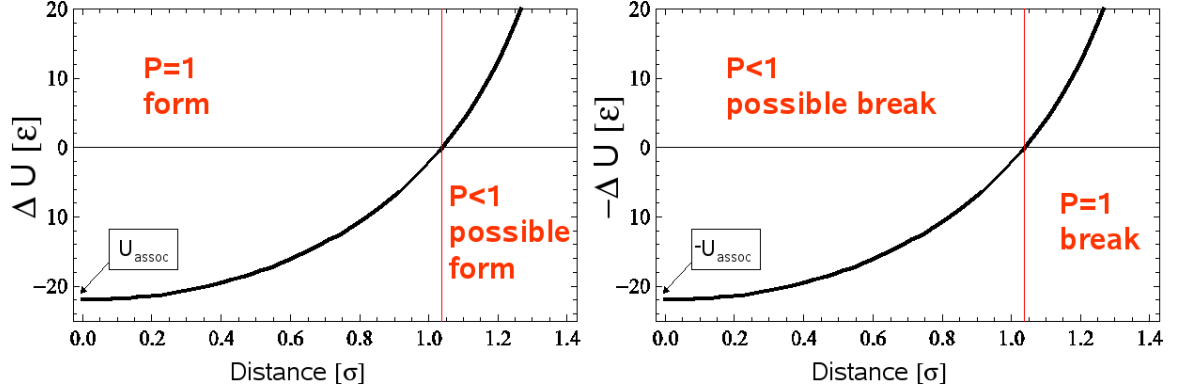
Figure 2.3: The energy difference Δ U for creation of a new junction between two endgroups (left) and for breaking an existing junction (right).

conditions in the x- and y-direction. The volume fraction of the simulation box that is occupied equals $\left(8000 \cdot \frac{4}{3} \cdot \pi(\frac{\sigma}{2})^3\right) / (23.69 \cdot 20.52 \cdot 27.84\sigma^3) = 0.309$. The atomic concentration is $8000/\left(23.69 \cdot 20.52 \cdot 27.84\sigma^3\right) = 0.591\sigma^{-3}$. A snapshot of the system is shown in figure 2.4. To keep the overview, only the endgroups of the polymer chains are shown. The coloring is representative for the size of the aggregate the endgroups is part of. At this temperature the average end-to-end distance of $< R >= 3.93\sigma$.

2.5   Temperature control

The desired temperature is reached through the friction coefficient Γ and the Gaussian white-noise source W_i in equation (2.1). W_i adds a random fluctuating force to the equation of motion and is Gaussian with average around 0. This takes into account the presence of the solvent in the system. The strength of the noise is related to Γ via the fluctuation dissipation theorem which quantifies the relation between fluctuations in a system at equilibrium and the response of the system to applied perturbations:

$$\langle \vec{W}_i(t)\vec{W}_j(t')\rangle = 6k_BT\Gamma\delta_{ij}\delta(t - t').$$ (2.23)

17

Therefore the system will take a temperature T depending on the strength of the fluctuating force that is applied. It is said the system is coupled to a heat bath.

Initially the system is set to $T = 1.5$ and no junctions are allowed by setting $U^{assoc} = 0$. Then U^{assoc} is gradually lowered to -22ϵ. Data at lower temperature is achieved by cooling the system at a rate of 2500τ per $\Delta T = 0.1$. Any phase transitions will not depend on cooling rate because of this slow cooling. At each T the system is sampled for at least 5000τ before statistical averages are calculated. After such a time the statistical averages and structural properties are equilibrated, but the system shows rich dynamics at a local scale since individual aggregates dissolve and new ones are formed. It was verified that the data obtained upon cooling and heating are identical within statistical errors. The positions of the atoms and the network structure are then typically recorded every 5τ.
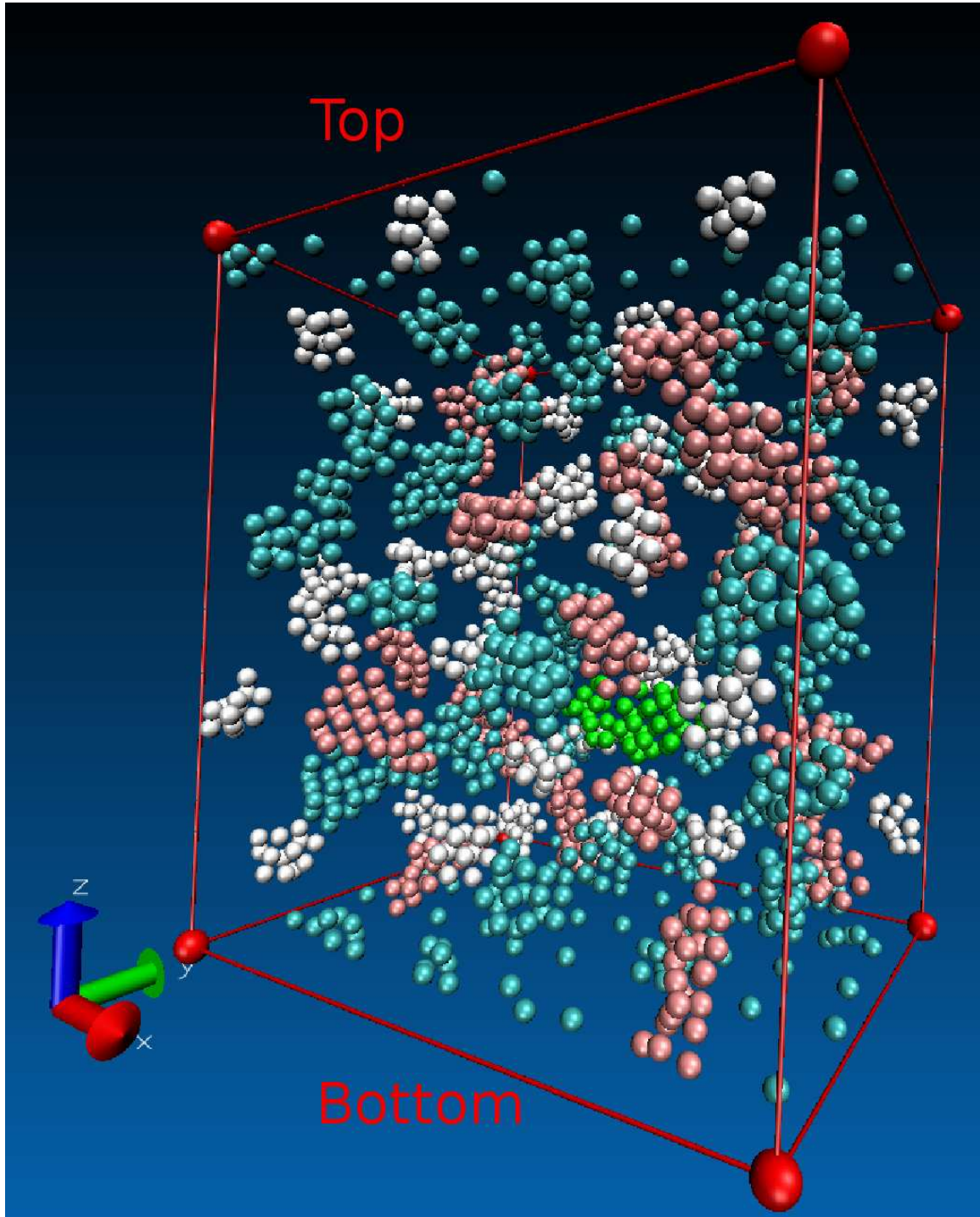
Figure 2.4: Snapshot of the system at T=0.35. The wall atoms are not displayed, but indicated by "Top" and "Bottom". The single endgroups on the bottom and top walls are the grafted ones. To keep the overview, only the 2000 endgroups are shown. The coloring of the endgroups denotes the size of the aggregate they are part of. Note that the system repeats itself in the x- and y-direction (not shown here).

Chapter 3

Topological study of the unsheared system using network theory

This chapter is a modified version of the paper "Topological changes at the gel transition of a reversible polymeric network" by J. Billen, M. Wilson, A. Rabinovitch, and A. R. C. Baljon, published in Europhysics Letters [21].

We use graph theory to quantify the topology of the simulated gel network (SGN). We will show that the topology changes as a function of temperature and point out differences above and below the micelle transition. Our analysis shows that the degree distribution of the system is bimodal and consists of two Poissonian distributions with different average degrees. The number of nodes in each of them as well as the distribution of links depend on temperature. By comparing the eigenvalue spectra of the simulated gel networks with those of reconstructed networks, the most likely topology at each temperature is determined. Topological changes occur at the transition temperatures reported in our previous study [19]. Below the micelle transition the topology can be described by a robust bimodal network in which superpeer nodes are linked among themselves and all peer nodes are linked only to superpeers. At

even lower temperatures the peers completely disappear leaving a structure of inter-connected superpeers.

3.1 Characteristic temperatures for the gel transtion

As mentioned before, at low temperatures the system undergoes a gel transition: due to the aggregates an extended network forms that prohibits flow. Since the volume fraction is approximately 30%, a glass transition, typically displayed in higher-density systems, is not observed. A previous study [19] has defined four characteristic temperatures for the gel transition. At low temperature the relaxation time as a function of temperature diverges either as a stretched exponential at $T_0 = 0.29$ or as a power-law at $T_c = 0.4$. Above $T_A = 0.75$ the dependence of relaxation time on temperature becomes of Arrhenius type. Geometric percolation occurs at high temperature of $T = 1.5$. Chapter 6 will study the percolation properties more in detail. At the micelle transition temperature $T_m = 0.51$ the number of reversible bonds ϕ strongly increases ($\frac{\partial^2 \phi}{\partial T^2} = 0$) and the specific heat peaks, characteristic for a second order phase transition. Below T_m the overall structure of the reversible network changes and a peak in the micelle size distribution becomes visible [19, 22]. Between T_m and T_0 collective modes of relaxation are still available to the system and cause a net flow over long time periods. In this chapter we investigate the structure of the SGN and how it changes with temperature. To this end, we compare it with that of complex networks found elsewhere in nature [23].

3.2 Complex network study of the polymeric gel

A complex network can be described as a set of nodes with links in between. In the well-known Erdös-Rényi (ER) random network [23], every pair of nodes is linked with
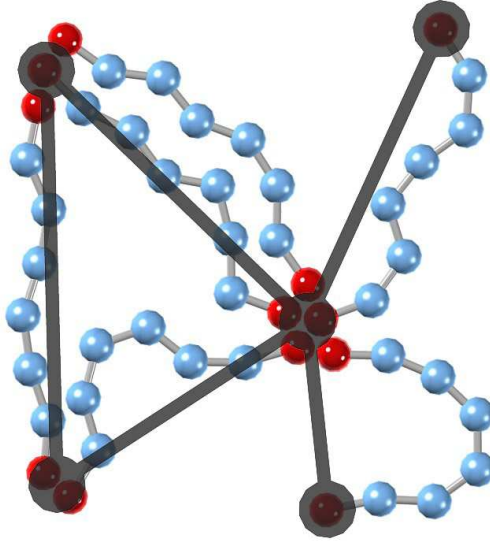
Figure 3.1: A 2D schematic illustrating the definition of nodes (black circles) and links (black lines) for a hypothetical bead-spring configuration. The beads at both chain ends are red and the others blue. Note that all simulations are performed in 3D.

a probability p. The degree distribution of this network, which describes the number of links k per node, is Poissonian:

$$P(k) = \frac{\langle k \rangle^k e^{-\langle k \rangle}}{k!} \tag{3.1}$$

The average degree $\langle k \rangle = Np = \frac{2l}{N}$, where l equals the number of links and N the number of nodes. In order to compare the simulated gels to other complex networks, we call an aggregate of endgroups a node. A polymer chain is identified as a link (unless both ends belong to the same aggregate). In a recent paper [24] a graph for reversible polymers was defined in the same way. In our simulations it is possible that the ends of more than one polymer chain connect the same pair of aggregates. If this is the case, we still count it as one link. Also it is possible that both endgroups of the polymer chain connect to each other (loops). These loops are not included in
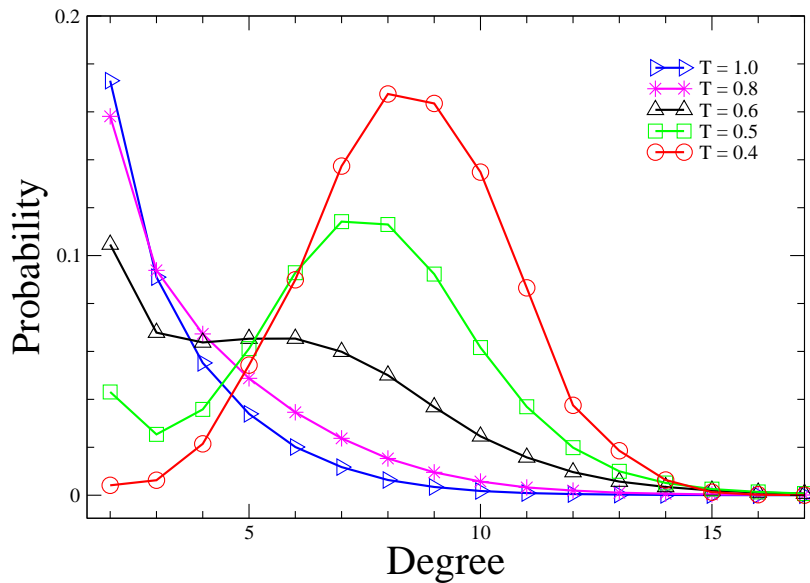
Figure 3.2: Degree distributions of the networks obtained from simulations at various temperatures.

the study, since they are not elastically active. A schematic picture illustrating the definition of a node and a link is shown in figure 3.1.

The degree distribution of the networks is shown in figure 3.2. The probability distribution is bimodal and qualitatively similar to the aggregate distribution of the model at hand [19] and to that reported by others [22, 25] for simulations of polymers with different chain lengths and interaction potentials. The goal of this study is to quantify the distribution and to characterize the topological changes using graph theory. As shown in figure 3.3 for $T = 0.55$, a superposition of two Poisson distributions with different values of <k> fits the data,

$$P(k) = n_S \frac{\langle k \rangle_S^k e^{-\langle k \rangle_S}}{k!} + n_P \frac{\langle k \rangle_P^k e^{-\langle k \rangle_P}}{k!} \tag{3.2}$$

Such a bimodal degree distribution is characteristic of complex networks which contain two types of nodes. Nodes in the distribution with the higher <k> value <k>$_S$
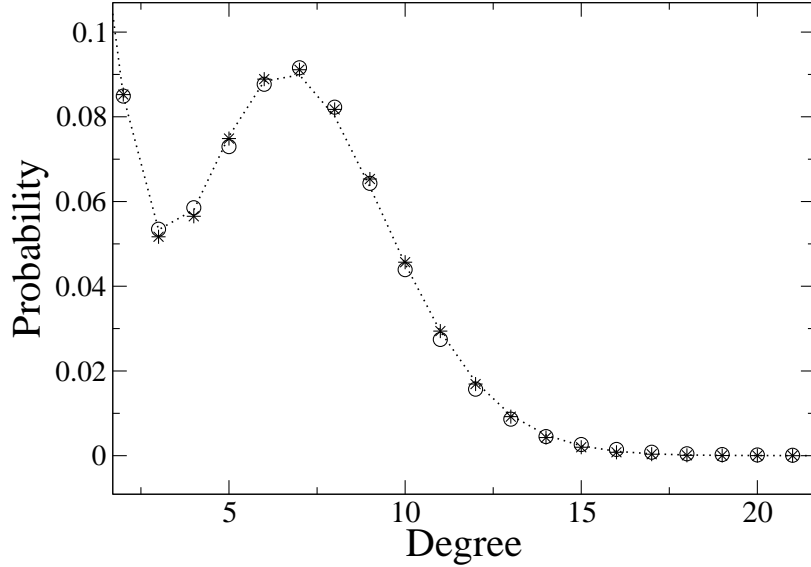
Figure 3.3: Degree distribution for T=0.55 (circles). The dotted line shows a fit to equation (3.2) using the values in table 3.1. The stars result from a reconstruction of the gel network as described in the text.

are called "superpeers" (S), those in the other distribution "peers" (P) [26]. n_S and n_P are the fractions of superpeer and peer nodes, respectively. Within the simulations links break and new ones form all the time. In such a dynamic network, nodes alternate between being part of the superpeer and peer distribution.

Table 3.1 lists the values of n_S, n_P, $<k>_S$, and $<k>_P$ of the fits to the SGN for a range of temperatures. With decreasing temperature n_S increases. Below T=0.4 n_P=0 and a single distribution of superpeers remains. The correlation coefficient (CC) of the fit is excellent at high temperatures, but becomes less accurate at temperatures below $T = 0.5$. We found that the single distribution below $T = 0.4$ has a slightly higher variance than predicted by a Poissonian model. Nevertheless, the data indicates that the SGN can be described by two Poissonians, whose relative contributions depend on temperature. This is shown in figure 3.4, where the fraction of superpeer nodes n_S is plotted. The inset shows its rate of change. This rate peaks
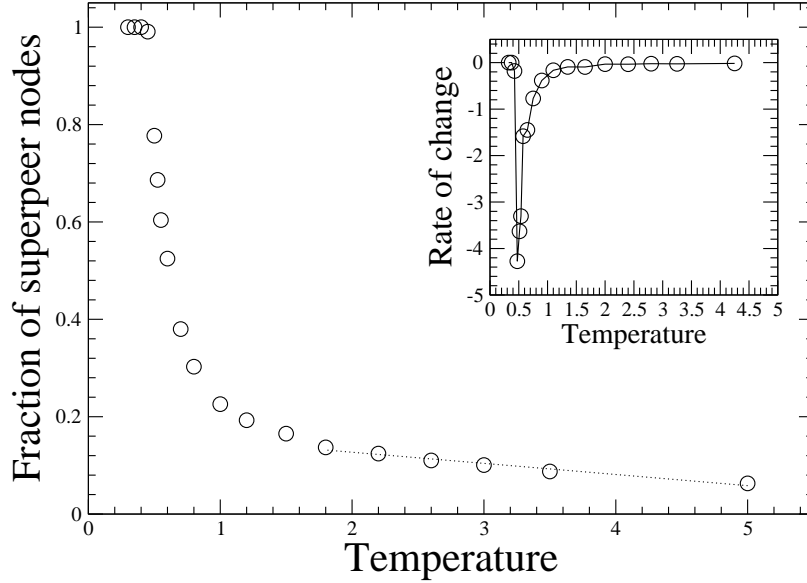
Figure 3.4: Fraction of superpeers as a function of temperature. The inset shows the rate of change of the fraction of superpeers.

at the micelle transition ($T = 0.5$). At this temperature there is a strong increase in the average aggregate size. Moreover, the data in figure 3.4 suggest that there is a qualitative change in the shape of their degree distribution and in the topology of the network structure.

3.3 Construction of related networks that mimic the gel network

To obtain further insight into these topological changes of the SGN with temperature, related networks (RN) were constructed according to the following recipe. At each temperature, we assign random coordinates in a 3D unit cell to N nodes maintaining the n_S / n_P ratio from table 3.1. Next, links are added in such a way that the desired values of $<k>_S$ and $<k>_P$ are obtained. To this end, the number of links between superpeers $l_{SS,}$ the number of link between peers $l_{PP,}$ and the number of

Table 3.1: Results of fits of degree distributions to equation (3.2)

T	n_S	n_P	$<k>_S$	$<k>_P$	CC
5.0	0.063	0.937	1.512	0.420	1.000
3.0	0.100	0.900	1.915	0.533	1.000
2.2	0.124	0.876	2.238	0.621	1.000
1.8	0.137	0.863	2.551	0.716	1.000
1.5	0.165	0.835	2.731	0.735	1.000
1.2	0.193	0.807	3.264	0.890	1.000
1.0	0.226	0.774	3.867	1.045	1.000
0.8	0.303	0.697	4.784	1.266	1.000
0.7	0.380	0.620	5.544	1.402	0.999
0.6	0.525	0.475	6.552	1.387	1.000
0.55	0.604	0.396	7.131	0.997	1.000
0.5	0.777	0.223	7.765	0.830	0.991
0.45	0.991	0.009	8.356	0.984	0.976
0.4	1.0	0.0	8.620		0.976
0.3	1.0	0.0	8.720		0.960

links between a peer and a superpeer l_{PS} are chosen such that:

$$
\langle k \rangle_S = (2l_{SS} + l_{PS})/n_S \\
\langle k \rangle_P = (l_{PS} + 2l_{PP})/n_P
$$

(3.3)

Initially, all links are chosen randomly. Further modifications are necessary given that the SGN is a spatial graph [23], because chain molecules that form the links have a finite size. They are approximately 7 σ long when fully stretched. Hence we allow only links between nodes that are shorter than a certain cutoff distance. The number of each type of link and hence the values of $<k>_S$ and $<k>_P$ are unchanged. To decide on the value of the cutoff distance, we calculate clustering coeffcients. For a particular node, the clustering coefficient is defined as the fraction of its neighbors that connect among themselves. The clustering coefficient of the entire network is obtained by averaging over all nodes of degree two and up [23]. Spatial dependence causes the clustering coefficient of a network to increase. Figure 3.5 shows the clus-
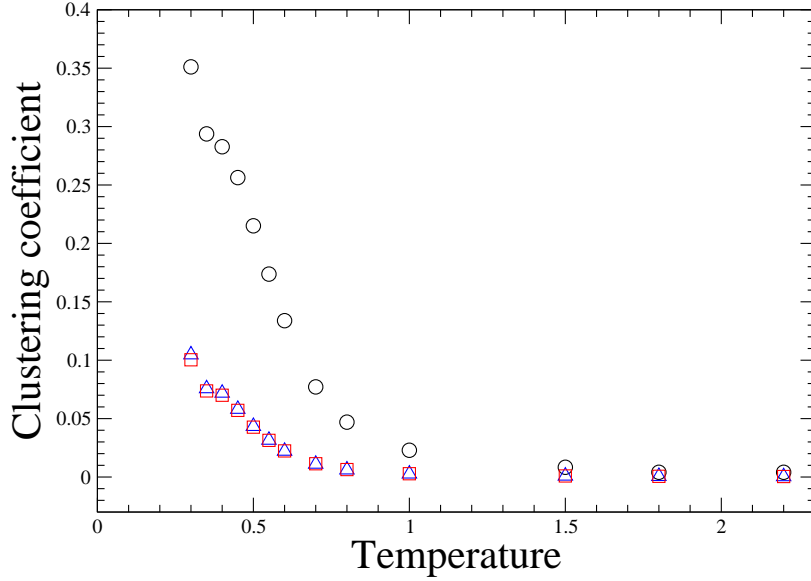
Figure 3.5: The clustering coefficient as a function of temperature. The circles are for the SGN. After rewiring the values change to those indicated by the blue triangles. The red squares are the calculated values from equation (3.5).

tering coefficient as a function of temperature for the SGN (circles). It turns out that the clustering coefficient of a graph with purely random links is much smaller than that of the SGN, as expected. A RN is constructed by adjusting the cutoff distance so as to match its clustering coefficient to that of the SGN. At $T = 0.55$ a cutoff distance of 0.28 is needed. Given the dimensions of our system this corresponds to 6.6σ . At higher T , the value of the cutoff distance slightly increases. The degree distributions of the RN are similar to that of the SGN (shown in figure 3.3 for $T = 0.55$). This finishes the description of the construction of the RN.

To further explore the relation between the SGN and random graphs we have investigated what happens to the clustering coefficient of the SGN when spatial dependence is removed. This task is achieved through a rewiring process in which links of restricted length are replaced by ones with arbitrary length in such a way that

the degree distribution is preserved [1] . During rewiring, the clustering coefficient decreases. Its steady state values are shown in figure 3.5 (triangles). Also shown is the theoretical value of the clustering coefficient [27] of an ER network with average degree <k>:

$$C = \frac{\langle k \rangle}{N} \left[\frac{\langle k^2 \rangle - \langle k \rangle^2}{\langle k \rangle^2} \right]^2 \tag{3.4}$$

where N, the total number of nodes, is matched to that observed in the SGN. As one can see, the clustering coefficients of the rewired SGN are very close to those predicted by this equation. We now further investigate the spatial dependent SGN using the RN for which the clustering coefficient was matched by restricting the length of allowed links. The network topology is quantified in more detail by the number of links and their distribution (l_{SS}, l_{PP}, and l_{PS}). There is still one degree of freedom in choosing these three numbers in such a way that equation (3.3) is satisfied. Hence another property is needed to decide which link distributions best mimic the simulated gel networks.

3.4 Eigenvalue spectra for studying topological changes

To this end, we calculate the spectral density $\rho(\lambda)$ of the adjacency matrix of a specific configuration of the SGN [28]:

$$\rho(\lambda) = \frac{1}{N} \sum_{j=1}^{N} \delta(\lambda - \lambda_j), \tag{3.5}$$

where the λ_j are the eigenvalues of the adjacency matrix. The results are averaged over 100 independent configurations of the SGN. The result is shown for $T = 0.55$ in figure 3.6(a). The spectrum of the SGN is then compared with that of RNs for a

---

[1]Starting with the configuration taken from the SGN, endpoints of two links are switched according to the following procedure: i) Randomly select links l_{hi} and l_{jk} connecting nodes n_h , n_i and n_j , n_k , respectively. ii) Remove links l_{hi} and l_{jk} , followed by the creation of new links l_{hj} and l_{ik} if none of these links already exist.
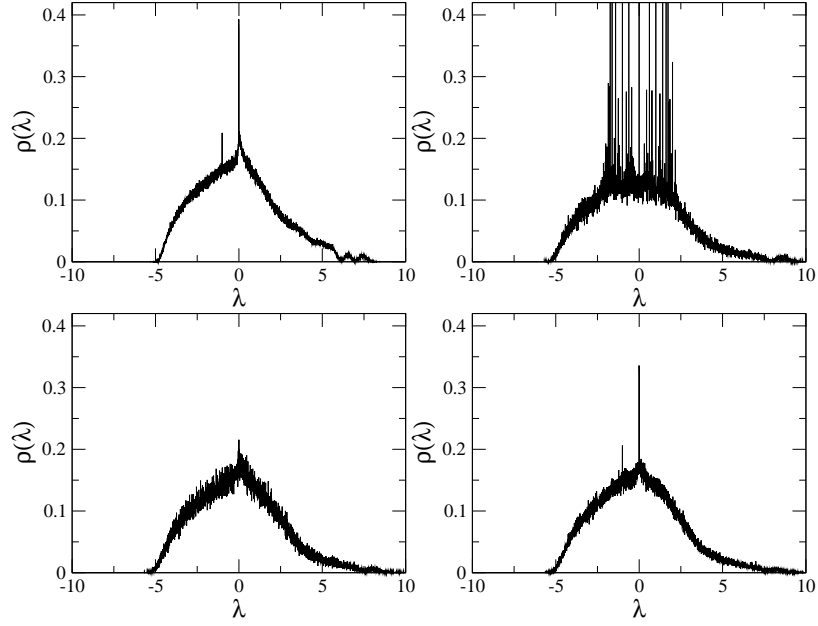
Figure 3.6: A comparison of the spectral density of of the SGN (a) with RN's (b, c, and d). In (b) the networks of peers and superpeers are disconnected (l_{PS}=0), (c) is for the case that peers do not link among themselves (l_{PP}=0), and (d) shows the RN that matches the SGN. In this case l_{SS}/l_{tot}=0.85±0.01, l_{PP}/l_{tot}=0.02±0.01, and l_{PS}/l_{tot}=0.13±0.01.

range of choices for the number of links, chosen such that equation (3.3) is satisfied. As seen in figure 3.6, when l_{PS}=0 and hence l_{PP} is maximum (b), the spectrum possesses many peaks. This is due to an abundance of disconnected clusters (groups of nodes linked together). The spectrum of a network in which l_{PP}=0 and hence all peers are only connected to superpeers (c) is the smoothest. In all cases the spectrum is asymmetric. As we report in chapter 4, this is due to the spatial dependence of the network. Without spatial dependence, ER networks are symmetric in the limit $N \to \infty$. We use the height of the peak at $\lambda = $ -1 as a criterion to determine the value of l_{PP} for which the RN spectrum best matches that of the SGN. As we show in chapter 4, the height of this peak depends on the number of triangles. A triangle is a structure in which three links connect three nodes. An increase in l_{PP} leads to an
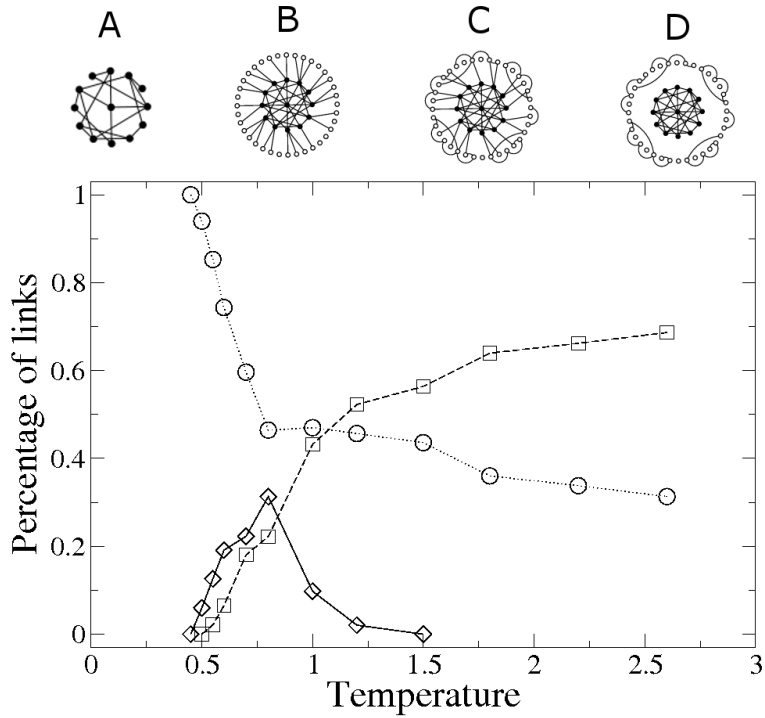
Figure 3.7: Percentage of each type of link as a function of temperature. Circles for l_{SS}/l_{tot} , squares for l_{PP}/l_{tot}, and diamonds for l_{PS}/l_{tot}. Lines are guides for the eye. The cartoons show the transitions in the peer-superpeer networks. Superpeers are shown as closed dots and peers as open dots.

increase in the number of triangles and hence in the peak height at $\lambda = $ -1. The best match is shown in figure 3.6(d). In this case l_{SS}/l_{tot}=0.85±0.01, l_{PP}/l_{tot}=0.02±0.01, and l_{PS}/l_{tot}=0.13±0.01. Here $l_{tot} = l_{SS}+l_{PP}+l_{PS}$. We found that the fractions of the "giant network component" [23] in the SGN and RN at these settings are comparable as well.

A similar comparison is performed for all temperatures. The results are shown in figure 3.7. Sketches of the peer-superpeer network are displayed as well. At the highest temperatures the system consists of two separate networks (D). If the temperature is lowered, links between peers and superpeers are formed (C). Gradually the number of peers and the number of links in between them decrease. At $T = 0.5$ the number

of links between peers vanishes and every peer is linked to a superpeer (B). Finally, below $T = 0.4$ only superpeers and links between them remain (A).

3.5   Conclusions

We conclude that during the transition from a fluid to a gel state the SGN undergoes several topological changes. These were studied by means of graph theory, considering aggregates as nodes and polymer chains as links. Construction of representative bimodal graphs (RN) has allowed us to investigate their topology in detail. Spatial effects were accounted for by restricting the size of links in such a way that the clustering coefficient of the RNs matches that of the SGNs. By comparing spectral densities, we were able to determine the number of links between peers and between superpeers, as well as those connecting peers to superpeers. We detected that significant changes in the topology occur at temperatures we have previously characterized [19] as transition temperatures. Most importantly, below the micelle transition temperature T_m = 0.5 links between the peers disappear. The resulting topology has been widely studied in the literature [29, 30] and was shown to be extremely robust. Moreover, below $T_c = 0.4$ the peer nodes themselves disappear and a single degree distribution remains. Given that the topological changes occur at the same temperatures as the rheological transitions observed in previous work, we believe that these effects could be intimately related.

Chapter 4

Eigenvalue spectra of spatial-dependent networks

This chapter is a modified version of the paper "Eigenvalue spectra of spatial-dependent networks" by J. Billen, M. Wilson, A. R. C. Baljon, and A. Rabinovitch, published in Physical Review E [31].

In the previous chapter we studied the eigenvalue spectrum of the polymeric gel. This revealed that because of spatial dependence, the spectrum was assymetric. In this chapter we will study in detail the influence of the spatial dependence on the spectral density of a network. Many real life networks exhibit a spatial dependence, i.e. the probability to form an edge between two nodes in the network, depends on the distance between them. When increasing spatial dependence in Erdös-Rényi, scale-free and small-world networks, it is found that the spectrum changes. Due to the spatial dependence the degree of clustering and the number of triangles increase. This results in a higher asymmetry (skewness). Our results show that the spectrum can be used to detect and quantify clustering and spatial dependence in a network.

4.1 Introduction

An increase in computational resources has led to a considerable interest in complex networks over the last decade. Initially most studies handled networks in the dimensionless network space. Many real-life networks however live in a geographic space in which it is more favorable to form edges between nodes that are close to each other. For this reason interest in these spatial networks (SN) has increased in the last few years. SN can be found in the fields of communication (Internet [32]), biology (neural networks [33]), transportation (airport [34, 35], rail [36], and road networks [34]), social networks [37] (friendships), and disease spreading [38]. To determine the existence of spatial dependency of a network one can look at several measures [34]. A spatial measure is the distribution of the Euclidean distance (ED) between nodes. In contrast, the so-called graph distance, measures the number of edges traversed along the shortest path from one vertex to another (path length). In this work we propose a more prominent method to detect spatial dependence based on the spectral density of a network. The eigenvalue spectrum of the adjacency matrix of a graph contains information related to important topological features of the graph. Therefore, it could also reflect the structural changes induced by spatial dependence. Eigenvalue spectra have been extensively studied for most common network models such as Erdös-Rényi (ER) random graphs, small-world networks, and scale-free networks [28]. In this work we study the influence of spatial dependence on the spectra of these networks in Euclidean space. In Section 2 we define the spectral density and its properties. In Section 3, the models are introduced. The resulting spectra are presented in Section 4. Section 5 discusses the results.

4.2 Eigenvalue spectrum of networks

The spectrum of a graph is the set of eigenvalues,λ_j, of a graph's adjacency matrix A [28]. The graphs under investigation are undirected and devoid of loops and multiple edges. Hence the adjacency matrix is real and symmetric, possessing real orthogonal eigenvalues [39]. The spectral density of a graph with N nodes can be defined as

$$\rho(\lambda) = \frac{1}{N} \sum_{j=1}^{N} \delta\left(\lambda - \lambda_j\right) \tag{4.1}$$

Since the spectrum contains all the topological information of the graph, it can be used to classify the network. The spectra of ER random, scale-free, and small-world structures in dimensionless network space have been studied extensively [28]. For the ER random network the spectral density exhibits a Wigner semicircle. The scale-free network displays a symmetric triangular bulk spectrum. A small-world network is constructed by placing nodes on a circle, connecting the k nearest neighbors and then randomly rewiring each edge with a probability p [40]. At $p = 0$ the small-world network has a regular structure and at $p = 1$ it becomes ER. The spectrum of the small-world network exhibits several peaks for small p values, because of its regularity [28] and it goes over to the semicircular shape when p approaches 1. The moments of the spectral density of a graph are related to its topology and the sth moment of $\rho(\lambda)$ can be written as

$$m_s = \frac{1}{N} \sum_{j=1}^{N} (\lambda_j - \mu)^s = \int (\lambda_j - \mu)^s \rho(\lambda) d\lambda \tag{4.2}$$

ince the spectrum contains all the topological information of the graph, it can be used to classify the network. The spectra of ER random, scale-free, and small-world structures in dimensionless network space have been studied extensively [28]. For the ER random network the spectral density exhibits a Wigner semicircle. The scale-free

network displays a symmetric triangular bulk spectrum. A small-world network is constructed by placing nodes on a circle, connecting the k nearest neighbors and then randomly rewiring each edge with a probability p [40]. At $p = 0$ the small-world network has a regular structure and at $p = 1$ it becomes ER. The spectrum of the small-world network exhibits several peaks for small p values, because of its regularity [28] and it goes over to the semicircular shape when p approaches 1. The moments of the spectral density of a graph are related to its topology and the sth moment of $\rho(\lambda)$ can be written as

$$m_s = \frac{1}{N} \sum_{j=1}^{N} (\lambda_j - \mu)^s = \int (\lambda_j - \mu)^s \rho(\lambda) d\lambda \tag{4.3}$$

with μ the mean eigenvalue. Since the adjacency matrix contains no loops, its trace will be zero and hence $\mu = 0$. $D_s = N m_s$ is the so called "number of directed paths of the graph that return to their starting vertex after s steps" [41]. Skewness and kurtosis are often used to describe shape characteristics of a distribution [42] and can be used to characterize the spectra. The skewness is a measure of the asymmetry of a distribution and is defined as:

$$S = \frac{m_3}{m_2^{3/2}} = \frac{N^{-1} \sum_i \lambda_i^3}{\sigma^3} \tag{4.4}$$

with $\sigma^2 = m_2 = <k>$ the standard deviation [23]. The kurtosis is K is a measure of the peakedness of a distribution and is defined as:

$$K = \frac{m_4}{m_2^2} - 3 \tag{4.5}$$

For a Gaussian distribution $\frac{m_4}{m_2^2} = 3$ and K=0. A semicircular distribution is known to have $S = 0$ and $K = -1$.

4.3 Construction of spatial ER, scale-free, and small-world networks in Euclidean space

To construct spatial ER, scale-free, and small-world networks, N nodes are randomly placed in Euclidean space in a $1 \times 1 \times 1$ box. Then l edges are created, favoring ones of shorter ED's, leading to a network with average degree $< k > = 2l/N$. Spatial dependence is obtained by choosing the probability $p_{i,j}$ to form an edge between 2 nodes i and j to depend on the ED $d_{i,j}$ between them:

$$p_{i,j} \propto \frac{d_{i,j}^{-\alpha}}{\sum_{b,c} d_{b,c}^{-\alpha}} \tag{4.6}$$

The strength of the spatial selection is determined by the value of the "proximity factor" α. When $\alpha = 0$ there is no spatial dependence. For $\alpha \to \infty$ only the closest edges will be chosen. We now discuss in more detail the construction method for each of the 3 networks under investigation. In our simulations we use $N = 1000$ and $l = 5000$ resulting in $< k > = 10$. All data result from averages over 100 configurations.

Table 4.1: Average ED for spatial-dependent networks.

α	0	2	4	6	8	10
ER/SW, $p = 1.00$	0.480	0.328	0.169	0.120	0.109	0.105
SW, $p = 0.75$	0.386	0.278	0.278	0.278	0.107	0.104
SW, $p = 0.50$	0.291	0.224	0.143	0.113	0.106	0.103
SW, $p = 0.25$	0.195	0.165	0.125	0.109	0.104	0.102
Lowest cost/ER $\alpha \to \infty$	0.100	0.100	0.100	0.100	0.100	0.100
SF	0.480	0.339	0.196	0.147	0.133	0.128

4.3.1 Spatial ER network

In a spatial ER network, each possible edge receives a connection probability as in equation (4.6) favoring nearby nodes ($\alpha > 0$). Once an edge is formed, the probability
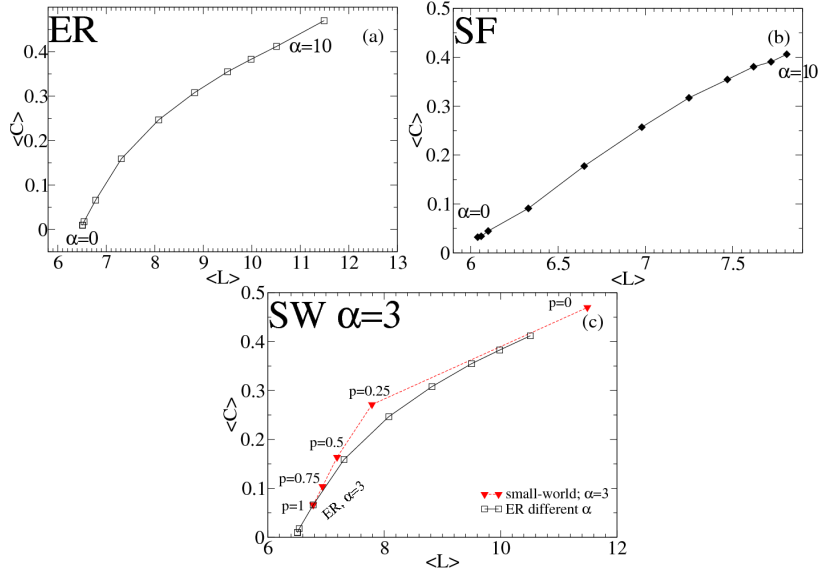
Figure 4.1: The average clustering coefficient over all nodes as a function of the path length for spatial dependent networks. (a) Random ER for different α. The data point for $\alpha \to +\infty$ corresponds to the lowest cost network. (b) Spatial dependent scale-free network for different α. (c) Small-world network for $\alpha = 3$ and $\alpha = 6$ for different p. For comparison data of figure 4.1a is shown as well.

for creating that edge is set to zero and the new probabilities are calculated. Repeating this process l times, a network with a Poisson connectivity distribution with a peak at $< k > = 2l/N$ is obtained. Alternatively we could have formed an edge between each pair of nodes with a certain probability p [23]. This would have given roughly the same results. Table 4.1 shows the average edge length for different values of α. For higher α shorter edges are formed. The clustering coefficient [43] as a function of average path length over all nodes is shown in figure 4.1a. The effect of proximity is visible by a strong increase in the clustering coefficient and a moderate increase in path length.

4.3.2 Spatial scale-free network

For constructing a spatial scale-free network we follow a procedure based on [44]:

- Select at random a subset of n_0 nodes and connect them. Nodes that have connections are called active.

- Take an inactive node i at random and connect it with an active node j with probability (up to a normalization factor)

$$p_{i,j} \propto (k_j + 1)d_{i,j}^{-\alpha} \tag{4.7}$$

where k_j is the degree of node j, and $d_{i,j}$ is the ED between nodes i and j. For each of the nodes, we repeat step 2) $m = 5$ times until all nodes are active. The degree distribution for $\alpha = 0$ shows a drop-off with a power law and $< k >= 2m = 10$. For large values of α the proximity effect limits the choice of available connections thereby limiting the degree distribution, resulting in a deviation from a power law behavior, as predicted in [44]. The effect of proximity is an increase in the clustering coefficient (figure 4.1b). The path length is smaller than that of an ER network due to the presence of hubs with a very high degree.

4.3.3 Spatial small-world network

In a dimensionless small-world (SW) network, a regular structure is obtained by placing N nodes on a ring and connecting each of them to its $< k >$ nearest neighbors [40]. Then each edge is rewired with a probability p. For intermediate p the system shows the small-world property, characterized by a small path length and a high clustering coefficient. For $p = 1$ the ER random network is obtained, exhibiting a small path length and a low clustering coefficient. For $p = 0$ the regular network stays intact. For the small-world network in 3D Euclidean space, we create a lowest cost configuration as the analogy of the regular structure. A lowest cost structure is found in brain networks where the cost of edges is optimized [45]. This structure is obtained by calculating the distance between all possible pairs of nodes, and connecting the

$N < k > /2$ ones that are closest to each other. The construction method for the spatial SW is therefore as follows:

- Calculate the ED between every possible pair of nodes, and connect the $N < k > /2$ closest ones. This is the lowest cost network.

- Consider rewiring each edge with a certain probability p. If rewiring takes place, the current edge is destroyed and replaced by a new edge while closer edges are favored depending on α according to equation (4.6). During the rewiring process, creation of every possible edge is allowed, but only once [1]. At the end of this rewiring cycle double edges can exist (except for $p = 0$ or $p = 1$).

- The "doubles" that exist after the rewiring cycle are now rewired, but this time only non-existing edges are allowed. Hence in the final configuration there are no multiple edges.

The network is completely determined by two parameters: the rewiring probability p and the proximity factor α. Note that the SW with proximity network for $p = 1$ and a certain α will correspond to the spatial ER for the same α. We see from figure 4.1c that the clustering coefficient for the small-world network is always higher than that for the ER for intermediate values of p. For $p = 0$ and $p = 1$ both networks have the same clustering coefficient. $p = 0$ is the lowest cost network with the shortest edges possible and is identical with the ER network with $\alpha \to \infty$. For $\alpha = 5$ similar results are found. Again, table 4.1 shows that for higher proximity, the average ED decreases.

---

[1]During the rewiring process, the formation of double edges is allowed. However during the construction, each edge can only be made once. Doubles are formed when the original edge is not rewired.
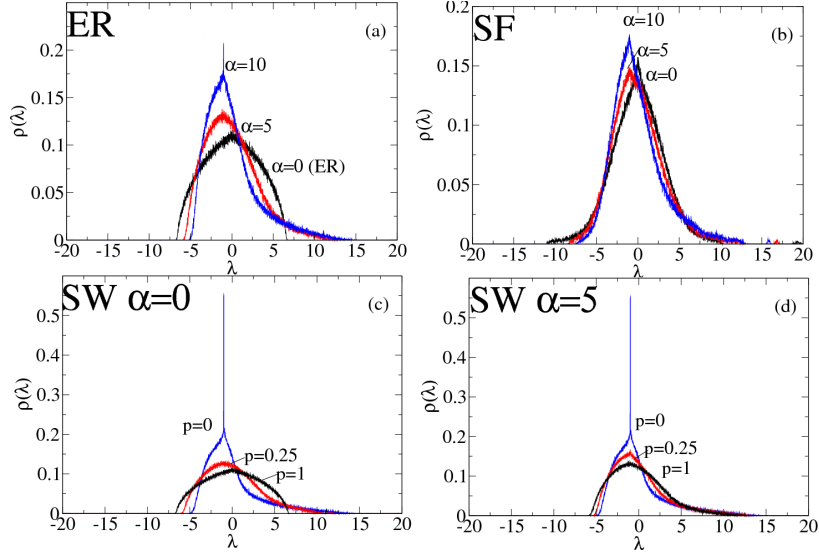
Figure 4.2: Eigenvalue spectra for spatially dependent networks: (a) ER, (b) scale-free, (c) small-world for $\alpha = 0$, (d) small-world for $\alpha = 5$.

4.3.4 Eigenvalue spectrum of spatial networks

The spectral densities for the ER random network for different values of α are shown in figure 4.2a. As expected for $\alpha = 0$ we find a semicircle. For $\alpha = 5$ the spectrum is asymmetric. The peak shifts to the left, and the right tail becomes fat. For $\alpha = 10$, -1 is the most abundant eigenvalue. The spectrum for the scale-free network is shown in figure 4.2b. Without proximity a triangular shape is found. For increased α the peak of the spectrum shifts to the left while the right-hand tail becomes fatter, and for $\alpha = 10$ the peak is at -1. The small-world network with no proximity is shown in figure 4.2c. $p = 1$ corresponds to an ER network. For lower p values the peak shifts to the left and the right tail becomes heavier. For the lowest cost network, $p = 0$, we find a peak at -1 and a very fat tail to the right. The small-world network for $\alpha = 5$ is shown in figure 4.2d. For $p = 1$ the small-world network again corresponds to the ER network with $\alpha = 5$. For decreasing p there is a transition to the lowest cost
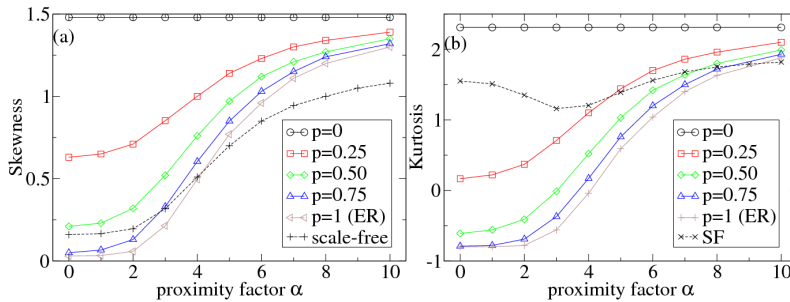
Figure 4.3: Skewness (a) and kurtosis (b) for spatial dependent networks.

network ($p = 0$), and the peak at -1 becomes more prominent. All spectra show an increased asymmetry with increased α. In order to quantify this effect we investigate the skewness S of the spectra in figure 4.3. For the semicircle the skewness is slightly higher than 0. This is due to the finite system size. As we will argue in Section 4, for $N \to \infty$, $S \to 0$ in an ER network. For increased α the network becomes more positively skewed and S increases. The lowest cost network shows the highest S. Next, we look at the peakedness in terms of the kurtosis K. For the small-world and the ER random networks, the kurtosis increases with α. For the semicircle K is close to -1 as expected. The lowest cost network has the highest K. For the scale-free network the kurtosis decreases for small α, and then increases for higher α.

4.4 Discussion

4.4.1 Skewness

To understand the observed asymmetry in figure 4.2 and the increase in skewness with α in figure 4.3a, we go back to the definition of skewness, equation (4.4). This can be transformed into:

$$S = \frac{D_3}{N\sigma^3} \tag{4.8}$$

Since $\sigma^2 = m_2 =< k >$ is independent of α, the skewness is directly dependent on the number of directed paths (DP) starting from a vertex and returning to that vertex after 3 steps, D_3. We studied the general D_s behavior for an ER network, a spatial ER network and the lowest cost network (fig. 4.4). The ER network with $\alpha = 0$ has a significant lower number of DP with odd s than DP of even s. This zigzag pattern is a consequence of the fact that, except for a few connections, a random graph looks like a tree and a tree has no DP of odd length. An ER network has no DP of odd length for $N \to \infty$ [28]. The number of DP with 2 steps $D_2 = N m_2 = N < k >$ is independent of α. As a result of the spatial dependence there is a strong increase in D_3 and D_5. We can understand the increase in D_3 with α (figure 4.4) by comparing the number of triangles T for the ER network with the number for a spatial network using a regular lattice. On a triangle one can define 6 directed paths (starting from each of the tree nodes and going either clockwise or counterclockwise).

Hence

$$D_3 = 6T \qquad (4.9)$$

where T is the number of triangles. A triangle consists of 3 nodes all having degree $k = 2$. Consider an ER network, and start from a specific node. There are on the average $\binom{<k>}{2}$ possible choices to pick 2 of its neighbors. The probability that these 2 neighbors are connected and a triangle is formed equals the total number of links $l = N < k > /2$ divided by the possible total number of possible links $N(N-1)/2$. Therefore the number of triangles in the ER network is:

$$T = \frac{N}{3} \frac{< k >!}{(< k > -2)!2!} \frac{N < k >}{2} \frac{2}{N(N-1)} \approx \frac{1}{6} < k >^2 < k - 1 > . \qquad (4.10)$$

The 1/3 comes from overcounting (each triangle has 3 corners). Combining equation (4.8)-(4.10) we find

$$S = \frac{< k >^2 < k - 1 >}{N \sigma^3} = \frac{< k >^{1/2} < k - 1 >}{N} \qquad (4.11)$$

42
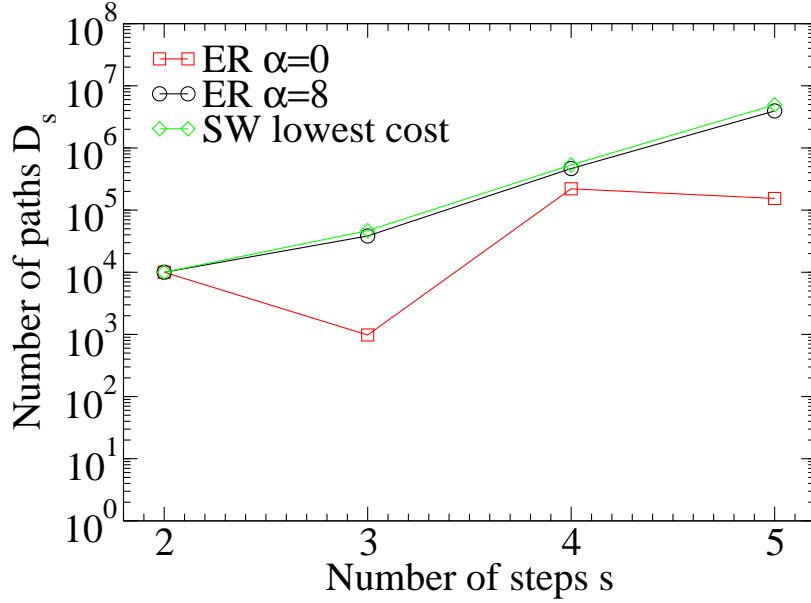
Figure 4.4: The number of directed paths D_s in an ER network without proximity (squares), with strong proximity ($\alpha = 8$, circles), and the lowest cost network (diamonds).

This shows that the non-zero skewness for the ER with $\alpha = 0$ in figure 4.3 is due to the finite system size. We have verified this finite-size effect numerically. We have also observed that in an "anti-proximity" network, where α is negative and distant edges are favored, $S \to 0$ for $\alpha \to -\infty$. We now consider the number of triangles in a network with proximity. Assume the nodes are placed on a 2D triangular lattice with coordination number $z = 6$ and that only nearest neighbors (NN) can be connected (lowest cost network). The number of triangles is different than the one for a simple ER network since the probability p that the two chosen neighbors are connected, is not the same. First of all the probability that the 2 chosen neighbors are NN of each other equals $\frac{2z}{z(z-1)} = \frac{2}{z-1}$. Second, the number of possible links equals $Nz/2$ in this case. Hence the number of triangles equals:

$$T = \frac{1}{3}N\frac{<k>!}{(<k>-2)!2!}\frac{2}{z-1}\frac{<k>}{z} = \frac{N}{3z(z-1)}<k>^2<k-1> \qquad (4.12)$$

For large N this is substantially higher than for the ER network. From equation (4.8)-(4.9)-(4.11) we find here

$$S = \frac{2 <k>^2 <k-1>}{\sigma^3 z(z-1)} = \frac{2 <k>^{\frac{1}{2}} <k-1>}{z(z-1)} \tag{4.13}$$

We note that the increase in clustering coefficient with proximity observed in figure 4.1 is also due to an increase in the number of triangles T. The clustering coefficient of a node i with degree k_i is defined as the number of triangles t_i in which vertex i participates normalized by the maximum possible number of such triangles [43]:

$$c_i = \frac{2t_i}{k_i(k_i - 1)} \tag{4.14}$$

In a system with N nodes the average clustering coefficient

$$\overline{C} = \frac{1}{N} \sum_{i=1}^{N} \frac{2t_i}{(k_i)(k_1 - 1)} \tag{4.15}$$

For large $<k>$, $k_i(k_i - 1)$ is sharply peaked around $<k_i(k_i - 1)>$. In this case

$$\overline{C} = \frac{1}{N <k_i(k_i - 1)>} \sum_{i=1}^{N} 2t_i = \frac{6T}{N <k_i(k_i - 1)>} \tag{4.16}$$

, where we have used that $T = \frac{1}{3} \sum_{i=1}^{N} t_i$, since each triangle contributes to 3 nodes. For an ER network with no spatial dependence, T is independent of N, hence both S and $\overline{C}$ are inversely proportional to N according to equation (4.11) and equation (4.15). The inverse dependence of $\overline{C}$ is a well known property [23]. For lowest cost networks, the number of triangles increases linearly with system size N and hence S and $\overline{C}$ are independent of system size. Further we have performed our analysis in two dimensions, but since equation (4.16) is dependent solely on the number of triangles we expect similar results for different dimensions.

4.4.2 Relation between skewness and clustering coefficient

By combining equation (4.8)-(4.16) and using $\sigma = <k>^{1/2}$ [23] it is observed that

$$S = \frac{6T}{N\sigma^3} = \frac{6T}{N <k>^{3/2}} = \overline{C} \frac{<k(k-1)>}{<k>^{3/2}} \tag{4.17}$$
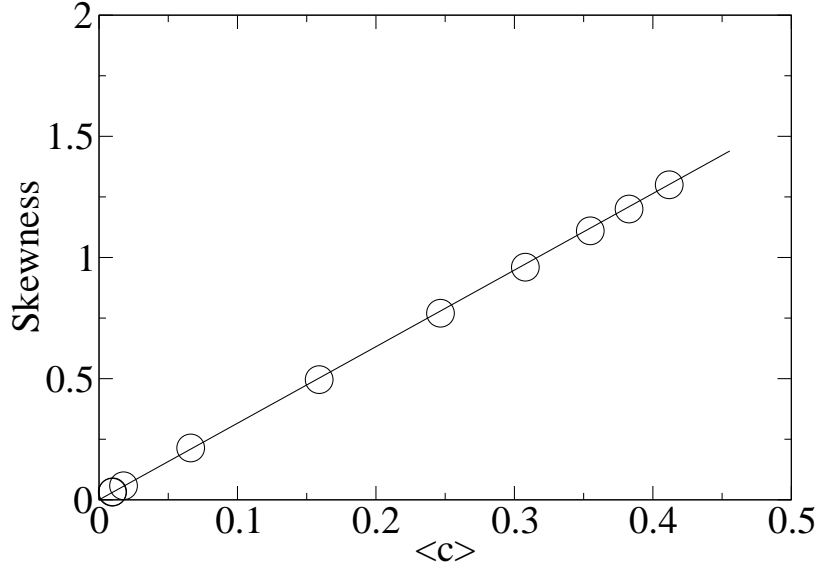
Figure 4.5: Skewness as a function of average clustering coefficient for the spatial ER network (circles). Equation (4.17) is added as a solid line with a slope of 3.16.

This shows that the skewness is an alternative measurement of the clustering of a network. We have numerically verified equation (4.17) by calculating the skewness as a function of the clustering coefficient for different values of α for the spatial ER network (figure 4.5). The measured values (circles) are in good agreement with the values predicted by equation (4.17) (solid line). For the scale-free network the condition under which equation (4.16) is a good approximation does not hold and we find a slope different than the one expected by equation (4.17). Asymmetry arises from the increase in the number of triangles in a network. Therefore, any method (not only the introduction of spatial dependence) which increases T would also increase asymmetry. For instance, increasing clustering in networks can be achieved by constructing a scale-free network in which, with a certain probability, the step of adding a node with preferential attachment is replaced by the creation of a triangle as described in [39]. We have constructed such networks and found indeed an increase in S, similar to the increase in the spatial ones.

45

4.4.3 The peak at -1

For all spatial networks it is observed that the spectrum peaks at -1 for high α values. This peak is also related to the observed increase in the number of triangles in the spatial network. To verify this hypothesis, we created an ER network and connected some of the dead-end vertices (nodes with degree 1) in two different ways. First, only dead-end vertices that are both connected to a common node were connected hence creating a triangle. Next, dead-end vertices were chosen at random and connected. For the first method we observed that the spectrum was a semicircle with a distinct peak at -1. The second method did not alter the semicircular distribution of the regular ER network. We conclude that the peak at -1 is induced by the spatial nature of the network. For high α this leads to the connection of nodes that are close to each other, resulting in an increase of triangles.

4.4.4 Kurtosis

We observed an increase in kurtosis with α for all SW and ER networks (figure 4.3b). For increasing α the peak grows and shifts to the left (figure 4.2). For the scale-free network, the kurtosis first decreases (figure 4.3b). This is the result of a combination of 2 effects. First, the pure scale-free network already has a sharp peak and hence high kurtosis around $\lambda = 0$. Second, for high α the degree distribution deviates from a power law (figure 4.1 in [44]). Hence the network is not scale-free anymore and the sharp peak decreases. Only at sufficiently high α values, the peak at -1 that is characteristic of spatial dependence appears and K increases again.

4.5   Conclusions

We have performed a study on the eigenvalue spectrum of spatial networks by modeling spatial ER, scale-free, and small-world networks. It was found that a positively skewed spectrum is a universal property of all spatial networks. We have shown that the increase in skewness is related to the increase in number of triangles in the system. We believe that the observed peak at -1 is also due to the increase in triangles. Our results show that the eigenvalue spectrum can also be used as a tool to detect clustering in a network. One way to achieve such clustering is by spatial dependence. The spectrum asymmetry is therefore a tool to study the degree of spatial dependence. The spectrum sheds more information on the network structure than measures such as ED distribution or path length. For instance, in the previous chapter the spectrum was used to determine the maximum length of an edge in a simulated polymeric gel [21].

Chapter 5

Simulations of associating polymers under shear

5.1 Introduction

In many systems, homogeneous flow is unstable above a critical applied shear rate or shear stress. The fluid may relax down to and maintain the shear stress plateau by separating into macroscopic coexisting bands of differing local viscosities and internal structuring. This phenomenon is called shear banding and has been observed in a wide variety of systems, such as emulsions, dispersions, granular materials, foams, telechelic polymers, and wormlike micelles (WMs). As mentioned in chapter 1, WMs are reversible breakable aggregates of surfactant molecules. As they are model compounds for polymers, shear banding has been most extensively studied experimentally in WMs [3, 46, 47, 48, 49, 50, 51, 52, 7]. Shear banding is usually observed using optical methods such as flow-induced birefrengence (FIB) [3], particle-image velocimetry (PIV) [3], light and small-angle neutron scattering (SANS) [46], and nuclear magnetic resonance (NMR) imaging [49].

One explanation for shear banding lies in the existence of multiple branches in the underlying constitutive curve relating shear stress to the shear rate $\dot{\gamma}$ in homogeneous flow, as shown in figure 5.1 [7]. The shear stress at first increases and then

drops behind a shear rate $\dot{\gamma}_M$, corresponding to the maximum of the $\sigma(\dot{\gamma})$ curve. If the applied shear rate lies in the decreasing part of the flow curve, the initially homogeneous flow becomes mechanically unstable. The mechanical characterization of such a non-homogeneous flow is the existence of a plateau $(\sigma(\dot{\gamma}) = \sigma_p)$ in the existing flow curve. Several non-monotonic rheological constitutive equations exist, and correspond to different competing models [53, 46, 47]. One such model is the Johnson-Segalman model [54], which leads to a modification of equation (1.4)

$$\sigma(\dot{\gamma}) = \frac{G\dot{\gamma}\tau}{1 + (1 - a^2)\dot{\gamma}^2\tau^2} + \eta\dot{\gamma} \tag{5.1}$$

with a a slip parameter, G a constant, and τ the relaxation time. The first term here is a viscoelastic term that causes the stress to decrease for intermediate $\dot{\gamma}$ due to the finite relaxation time of the system. For low and high $\dot{\gamma}$, the stress increases monotonically and homogeneous velocity profiles are expected. The lever rule state that the interface between both bands increases gradually with the shear rate while the local shear rates in both bands are constant. The average of the local shear rates in the bands must be that of the applied bulk shear rate:

$$\dot{\gamma} = \alpha_1\dot{\gamma}_{c1} + \alpha_2\dot{\gamma}_{c2} \tag{5.2}$$

where $\alpha_1 + \alpha_2 = 1$. Although some experiments confirm the lever rule [51, 47], others indicate that the the bands still grow in time once the constant stress in a transient measurement has been reached [3] and that the interface position strongly fluctuates with time [52, 49]. Also, it has theoretically been shown using the Johnson-Segalman model, that the picture of two stable bands separated by a stable interface is insufficient to explain the complex behavior at the interface [55].

Shear banding in telechelic polymers has been studied more recently [56, 2, 57]. From these studies, it is clear that the picture of two bands, separated by a smooth

interface that increases linearly with shear, is oversimplified. Sometimes three bands are observed and the behavior depends strongly on many parameters (temperature/atomic concentration, chemical structure, relaxation times of materials) [56, 17] along with the details on how the flow curve was obtained [2]. Shear banding is a complex problem that is still poorly understood.

Simulations can help in shedding new light on some aspects of the problem. They allow us to study several properties on the microscopic scale that are impossible to measure experimentally, such as the weight of the links in the network, the aggregate size distributions, the lifetime of a junction, atomic concentration, etc. The goal here is to verify the existence of shear banding within the system and investigate if any differences between the bands are inherent to the formation of the two shear rate bands. To our knowledge, simulations have not yet focused on these properties specifically in the scope of shear banding.

Next, we will address some other effects of shearing the simulated system. As explained in chapter 3, each polymer chain in our system can either form a loop or a bridge. If both endgroups of the chain are part of the same aggregate, a loop is formed. If both endgroups are part of different aggregates, the polymer chain bridging those aggregates will be referred to as a bridge. There are reports of an increase in number of loops under application of shear in simulation [58]. The loops then form flowerlike micelles connected by bridgelike chains. Because of the abundance of the looplike chains, the internal stress in the network decreases. Experimentalists often explain such a drop in terms of an increase in loops and a decrease in elastically active bridges [10, 2]. Other topological differences could also occur under shear. For example, aggregates could be linked by more chains on average. This would also lower the number of links. By assigning a weight to each link (the number of bridging chains it consists of), we will investigate changes in the strength of the network. This
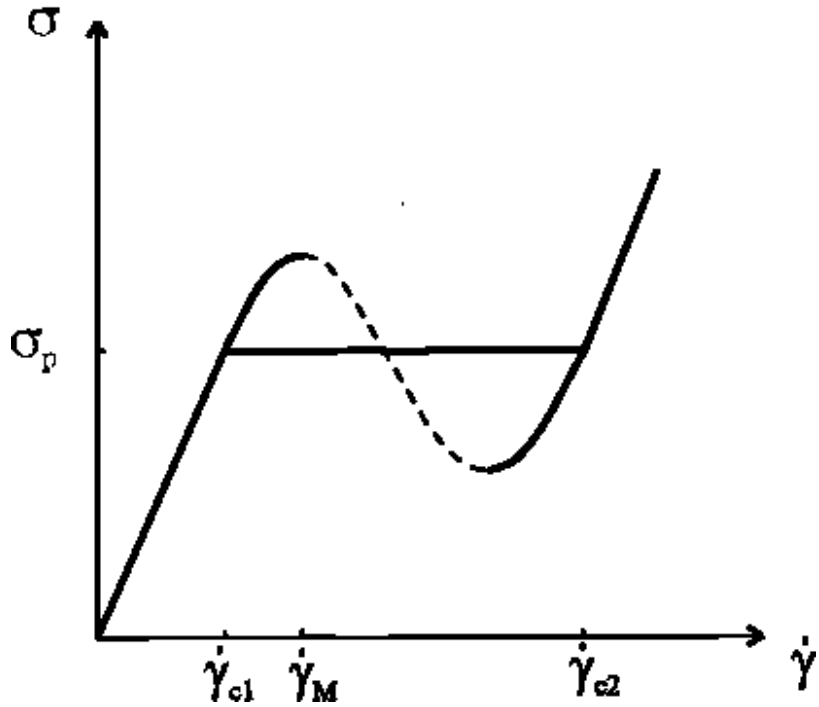
Figure 5.1: Schematic representation of a non-monotonic flow curve exhibiting plateau behavior indicative of shear-banding, taken from [3]. The dotted part corresponds to an unstable flow.

is experimentally impossible and to our knowledge, has never been taken into account before.

5.2   Methods

5.2.1   Application of constant shear and stress response

All results are at a temperature $T = 0.35$, well below the micelle transition. The top wall is moved with a velocity v. 5% of the polymer chains are permanently grafted to the top wall in order to shear the whole system. Hence the shear rate is $\dot{\gamma} = \frac{v}{h}$. A constant shear rate is applied that is varied between $1.79 \times 10^{-6} \tau^{-1}$ and $3.58 \times 10^{-2} \tau^{-1}$. The relaxation time of the system, obtained from diffusion data in earlier work [19] is

equal to $9.455 \times 10^{-8}\tau^{-1}$. Hence, all shear rates under consideration are larger than the inverse relaxation time and the system is in a non-equilibrium state. The force F required to move the upper wall is obtained from interactions between the wall atoms and the polymer beads. The shear stress is defined as

$$\text{Shear stress} = \frac{F}{A} \qquad (5.3)$$

with A the wall area. A transient stress response is then obtained by applying a constant shear rate to the system for a long time and continuously measuring the stress. Such a transient stress response is often shown as a function of shear strain, which is the deformation in the x-direction divided by the distance between the two walls, $h = 27.84\sigma$.

5.2.2 Velocity profiles

To calculate velocity profiles, the distance traveled in the x-direction by each individual atom in the gel is recorded over a time interval $\Delta t = 2500\tau$. The resulting velocities are binned in 56 slabs of thickness $0.5\ \sigma$, according to the average of the particle's initial and end location in the z-direction. In this way, several (typically 19) consecutive velocity profiles are recorded, and the time average of these different profiles over 50000τ is calculated.

5.3 Results

5.3.1 Stress response

The stress, is shown in figure 5.2. For low strain the response is linear. This is followed by a stress maximum which corresponds to the yield point. The maximum occurs at a strain of 1.5 σ, independent of shear rate. These results are in agreement with experiments on triblock copolymers [10], where it is shown that the position
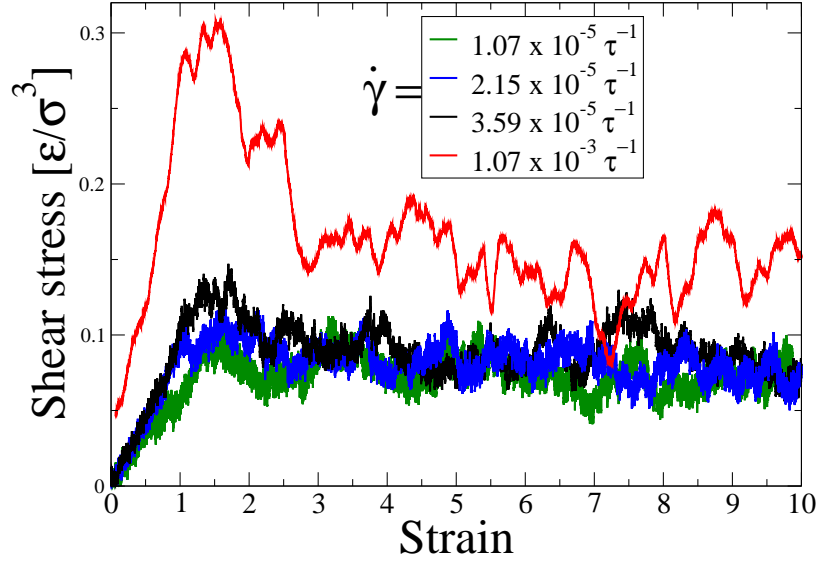
Figure 5.2: Stress response for $\dot{\gamma} = 1.07 \times 10^{-5}\tau^{-1}, 2.1 \times 10^{-5}\tau^{-1}, 3.59 \times 10^{-5}\tau^{-1}, 1.07 \times 10^{-3}\tau^{-1}$.

of the stress peak is determined by the length of the polymer backbone. Consistent with [59], our simulations show a stress overshoot. Once this peak is overcome, we see that the system yields and the stress drops (strain softening [10]) and fluctuates around an average value. Such fluctuations have been reported in experiments on telechelics as well [2, 57]. The average stress as measured after the peak for each shear rate is shown in figure 5.3. At low shear rates below $\dot{\gamma} = 3.59 \times 10^{-4}\tau^{-1}$, the average stress only sligthly increases over a two orders of magnitude increase in the shear rate. For higher shear rates, the stress strongly increases. A fit shows a slope of 0.08 in the plateau regime. Most experiments show a significant positive slope in the stress-plateau regime both for WMs [50, 51, 47, 48, 52], and for telechelics [2].
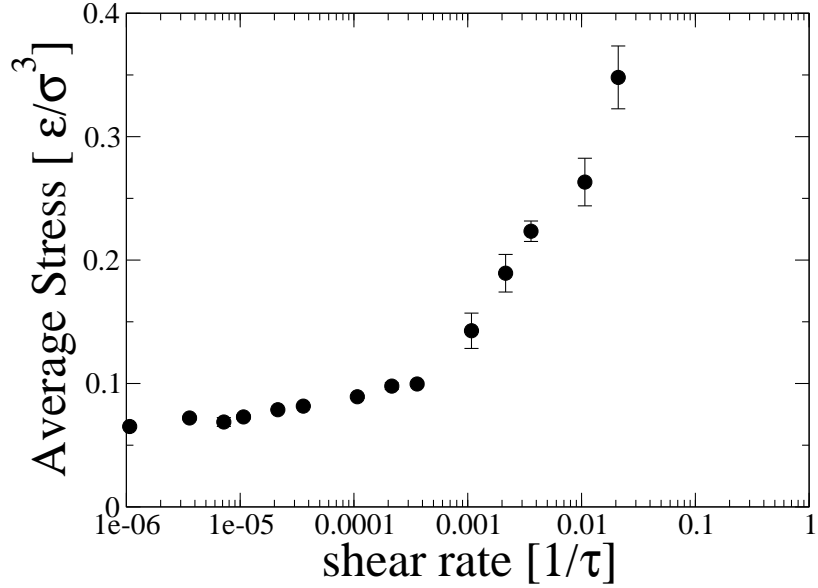
Figure 5.3: Average stress taken after the stress peak. Below $\dot{\gamma} = 3.59 \times 10^{-4}\tau^{-1}$ there is a plateau-like regime with slope 0.08.

5.3.2 Shear banding

Shear bands were most clearly visible for $\dot{\gamma} = 3.59 \times 10^{-4}\tau^{-1}$. Figure 5.4 shows the velocity profile of the particles in x-direction as a function of the distance perpendicular to the moving wall. The result is obtained by averaging over 7 equivalent runs that were cooled from different configurations at high temperature and subsequently sheared. This averaging was necessary since single velocity profiles were found to show complex behavior, with slightly different shear rates in both bands and a chaning location of the interface. There exist two regions of different slope below and above $17.1 \pm 0.5\sigma$. The shear rates in both bands are only a factor of 4.3 different ($\dot{\gamma} = 1.6 - 7.11 \times 10^{-4}\tau^{-1}$), which is close to what is found in experiments on telechelics [2], but less than observed for WLM [47]. When looking at a wide range of shear rates, the study of many velocity profiles was necessary. There was a lot of variation in shear rates in both bands, position of the interface, occurrence
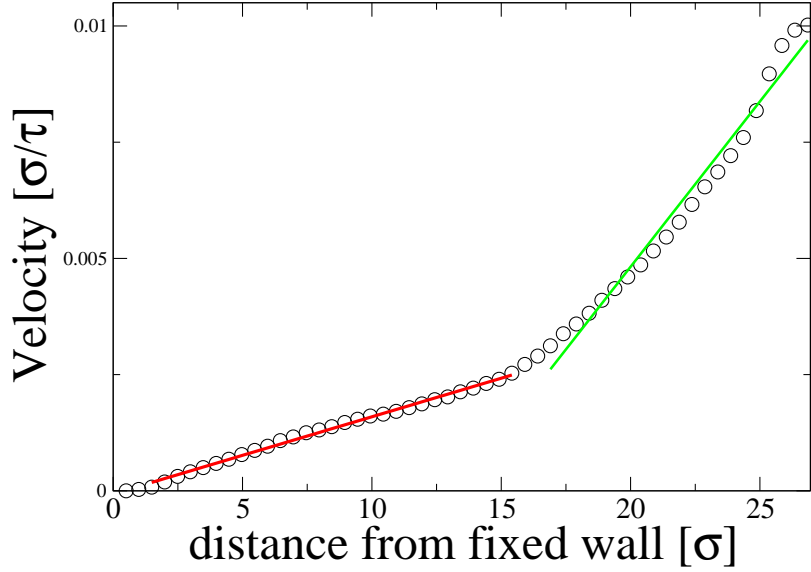
Figure 5.4: Velocity profile for $\dot{\gamma} = 3.59 \times 10^{-4}\tau^{-1}$ showing two regions of different shear rate. The shear rate in the low shear rate band is $\dot{\gamma}_1 = 1.6 \times 10^{-4}\tau^{-1}$ and the high shear band is $\dot{\gamma}_2 = 7.11 \times 10^{-4}\tau^{-1}$.

of shear banding (sometimes two bands only existed over a certain time interval, or three bands were observed). We concluded that we did not find clear evidence of the lever rule as the interface position did not increase significantly with increasing shear rate. As mentioned already in the introduction, also experiments report on a complex shear banding scenario in telechelics where the lever rule does not hold [56, 2].

5.3.3   Microscopic differences between shear bands

Table 5.1 shows a comparison of several microstructural quantities between the unsheared system, the low shear rate band, and the high shear rate band for $\dot{\gamma} = 3.59 \times 10^{-4}\tau^{-1}$. Data in the low and high shear rate band are obtained from averages over slabs between 1.8 and 5.8 σ from the walls. We observed strong spatial fluctuations in the interface over time, in agreement with experiments [56]. There-

fore, the slabs are chosen at a safe distance from both the time-averaged interface and the wall, the latter in order to exclude wall effects. As expected, a stretching of the chains causes a strong increase in end-to-end distance R^2 under shear. The stretch is identical in both bands, though. The bead concentration is not affected by shear. However, the high shear rate band contains more aggregates, but many of them consist of a single endgroup. A more detailed comparison of the aggregate sizes in the unsheared system and in both shear bands is given in figure 5.5, which shows the aggregate size distribution. As expected in the unsheared gel state the distribution peaks around a preferred value of 16 end groups. After the application of shear this value increases to 22. Such shear-induced aggregation has been reported previously as other simulations of self-associating polymers observed a widening of the aggregate size distribution [58]. In experiments on WMs the formation of larger size aggregates has been suggested, although only in the high shear rate band [52]. Besides shear-induced aggregation also the breaking of smaller aggregates (fewer than ten endgroups) is enhanced. This effect is most outspoken in the high shear rate band, which is the main difference between the distributions for low and high shear rate band. A measure for the dynamics of the system is the average lifetime of a junction.

Table 5.1: Overview of microstructural differences between unsheared and low and high shear rate band for $\dot{\gamma} = 3.59 \times 10^{-4} \tau^{-1}$.

Property	unsheared	low shear rate	high shear rate
$\langle R^2 \rangle \ [\sigma^2]$	15.45 ± 0.10	23.15 ± 0.90	22.65 ± 0.50
bead concentr. [beads/σ^3]	0.62 ± 0.01	0.62 ± 0.01	0.61 ± 0.01
agg. density [10^{-3} agg/σ^3]	8.62 ± 0.04	7.90 ± 0.04	8.94 ± 0.15
average agg. size	17.90 ± 0.16	19.66 ± 0.23	17.82 ± 0.56
agg. size 1 [10^{-4} agg/σ^3]	1.030 ± 0.115	5.030 ± 0.151	7.941 ± 0.103
junction lifetime [kτ]	$1\ 895 \pm 153$	11.22 ± 3.14	3.645 ± 0.625

Therefore, we measure the ratio of the junctions that survive over a given time inter-
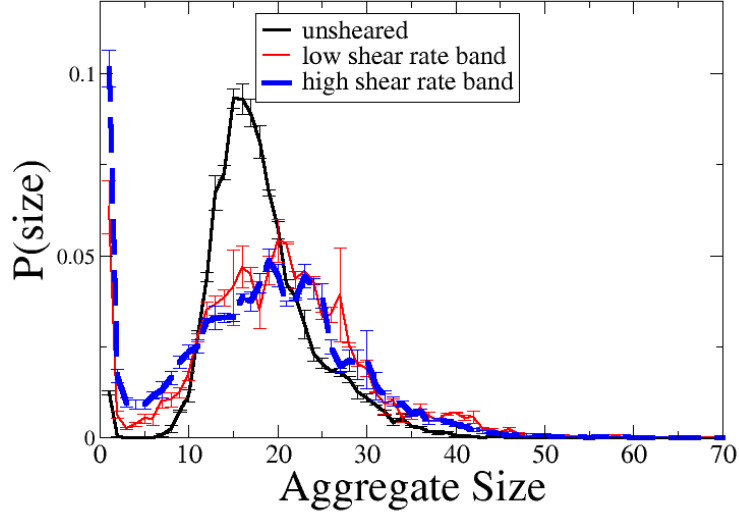
Figure 5.5: Aggregate size distributions for unsheared system (solid line), low shear band (dot-dash line), and high shear band (thin line) for $\dot{\gamma} = 3.59 \times 10^{-4}\tau^{-1}$.

val Δt. The lifetime is now defined as the time after which $1/e$ of the initial junctions survive. It is important to note that if two endgroups were separated temporarily but reunite later, the junction is still counted as surviving under the condition it is present at Δt. This means we consider the "effective lifetime" of a junction [60, 61], which can be thought of as the average time for the initially bonded junction to no longer recombine. This is of interest because it is typically measured in rheological experiments. The result of shear is a strong increase in dynamics which results in a decrease in lifetime of two orders of magnitude. This effect is strongest in the high shear rate band. We found that all the properties described above point out a difference between both shear rate bands. However the change is gradual as a function of the distance between the walls, rather than a sharp change at the interface.

5.3.4   Loop/bridge ratio and weight of the links

It is often mentioned that under shear a large fraction of the chains connects with both ends contained within the same aggregate (loop) instead of bridging between aggregates (bridge) [57, 10]. The number of loops and bridges is shown in figure 5.6. For $\dot{\gamma} = 3.59 \times 10^{-4}\tau^{-1}$, about 5% of the number of bridges are transferred into loops during the simulation time, but this occurs gradually and especially for high values of the strain, when the system is yielding. The drop in number of links is much more abrupt and occurs simultaneously with the stress overshoot and subsequent drop in figure 5.2, as indicated by the arrow. For low strain, the number of bridges barely changes and there are fewer links than with no strain. This means that the aggregates become linked by a higher number of bridging chains. We define the weight of a link as the number of bridging chains between the two aggregates.

Figure 5.7 shows the link weight distribution for the sheared system gathered after the yield peak, together with the distribution of the unsheared system. It is clear that there are more links of large weight under shear. The crossover from a higher probability to find a link of a certain weight in the sheared than in the unsheared system, takes places at weight = 3. The "weak" links, consisting of only a single or a double bridge, are ruptured easily and decrease under shear. The maximum weight that is found in a link in the the system increases with shear rate from weight = 6 (unsheared) to weight = 16. We conclude there are two processes as result of the shear. Initially the system strongly reorganizes. Since the number of bridges only slightly changes, many weak links disappear in favor of growing strong links. For large strain rates, this resilient network slowly turns bridges into loops. Our results verify the experimentally hypothesised change in loop/bridge ratio, but since this only occurs at high strain rates, the change in link weight distribution needs to be taken
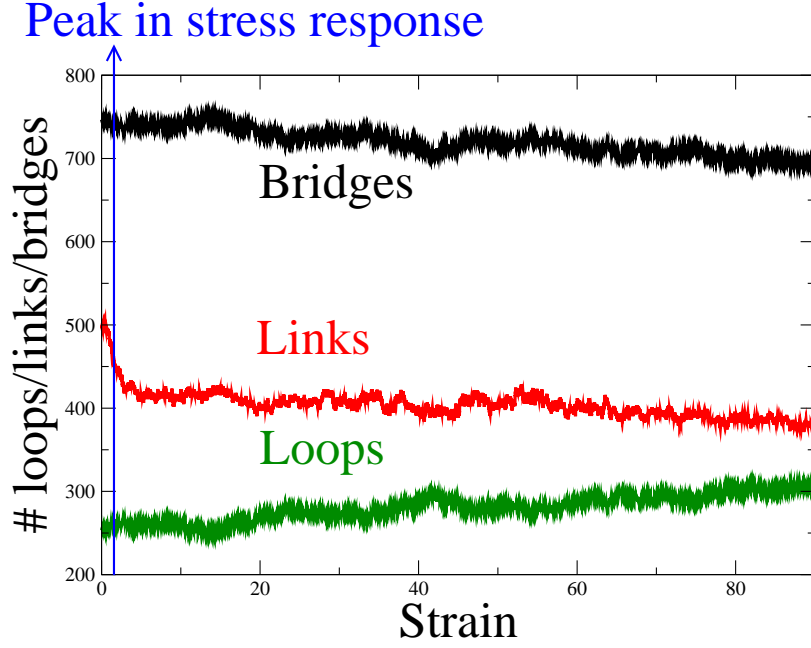
Figure 5.6: Evolution of number of bridges, links, and loops in the system for $\dot{\gamma} = 3.59 \times 10^{-4} \tau^{-1}$. A loop is a chain where both endgroups form a junction. A bridge is a chain that bridges two aggregates. A link is a connection between two aggregates and can consist of multiple bridging chains. The number of bridges linking two aggregates is the weight of the link.

into account to explain the decrease in stress response once the system is yielding. This idea is supported by the inset in figure 5.7 which shows the change in average weight

$$\langle w \rangle = \sum w P(w) \tag{5.4}$$

under shear. $\langle w \rangle$ increases as soon as the shear is applied. The formation of such a system consisting of links of high weight, is a direct result of the shear-induced aggregation. This can be seen by studying the relation between the average size of two aggregates that are connected, and the weight of the link between them, shown in figure 5.8. The weight of the link increases linearly with the aggregate size. Recent studies in our group show that the larger the link weight, the more it is aligned with
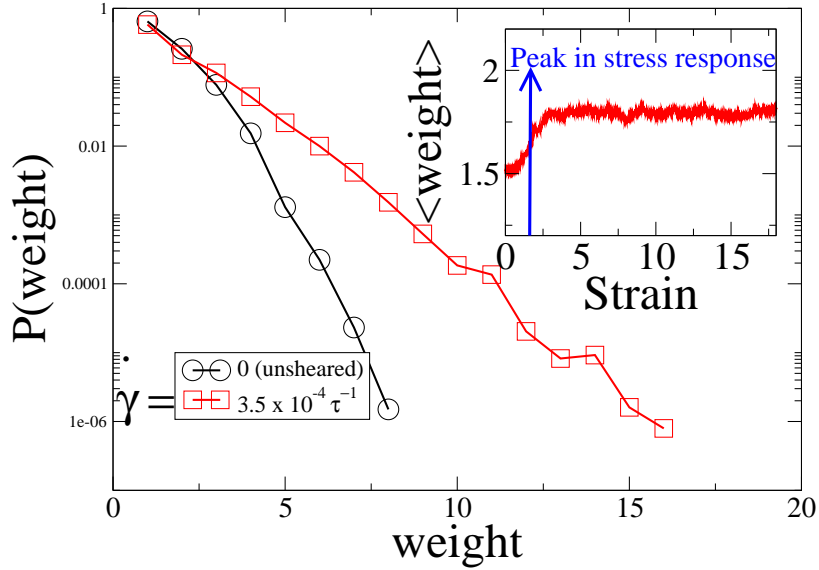
Figure 5.7: Link weight distribution for unsheared and $\dot{\gamma} = 3.59 \times 10^{-4}\tau^{-1}$. The inset shows the increase in $\langle weight \rangle$ which corresponds to the peak in the stress response.

the bounding walls (not shown here). This alignment does not occur for the unsheared system, for which the orientation of the chains with respect to the walls was random. Hence we envision a topology in which layers of aggregates are connected by strong links with many chains parallel to the walls. Weaker links with a few chains, that are more easily broken, connect in between these layers. Such layering of aggregates has been indeed observed in aggregate density profiles (not shown here).

5.4   Conclusions

We applied a wide range of shear rates to the system and observed a region in the shear-stress curve where the shear only slightly increases. Within this region, shear banding was observed. The interface between both shear bands fluctuates over time and our results confirm that the lever rule does not hold in telechelics.

Several microstructural changes were observed between both shear bands. Under
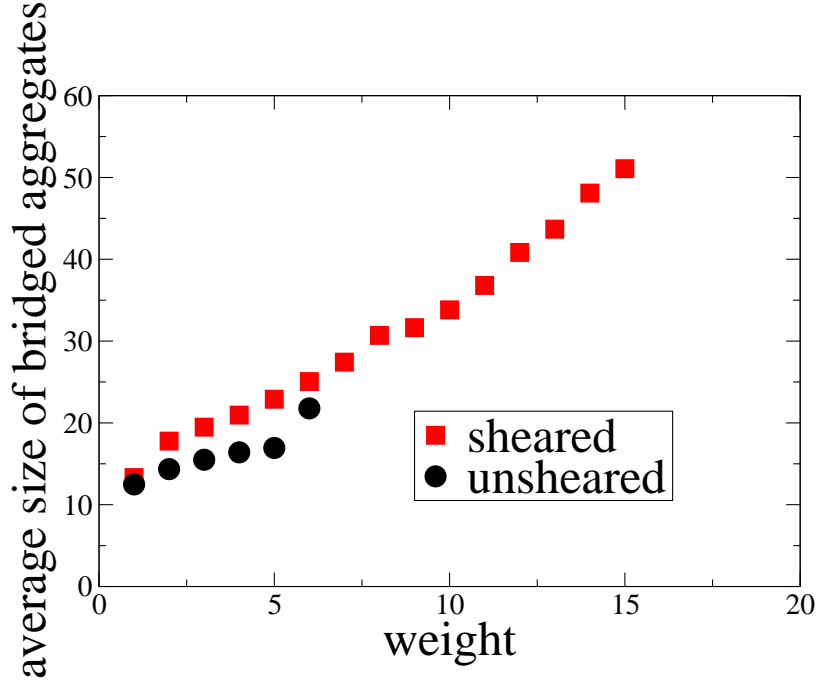
Figure 5.8: The average size of two aggregates as a function of the weight of the link in between them for $\dot{\gamma} = 3.59 \times 10^{-4}\tau^{-1}$.

shear there is a strong increase in dynamics, as indicated by the reduction of the effective lifetime. This effect is stronger in the high shear rate band and therefore, many aggregates consisting of a single endgroup are created. This results in more aggregates in the high shear rate band, but since many of them only consist of one endgroup, the average size is lower. The gradual change of these properties as a function of distance to the moving wall indicate that the reason for those differences are more likely to be the strong increase in dynamics, rather than inherent structural differences between both bands.

We found a change in topology as a function of shear. The size distribution of the sheared system indicates shear-induced aggregation: the system looses its preference to form aggregates of a specific size and the formation of larger and smaller size aggregates is enhanced. The resulting bimodal distribution is known to be more

robust against failure [29] than a single-peaked distribution, suggesting shear induces a structural change into a more resilient network. This picture is verified by investigating the weights of the links. As soon as the shear is applied, there is a decrease in the number of links in the network. The aggregates that are only weakly linked and have a weight lower than three, rupture more easily. The aggregates that are strongly connected with weight higher than three, grow and get connected stronger. Our results are of importance in the light of recently developed models that describe a stress drop as a result of a decreased bridging factor [57, 10]. We find indeed that a signifcant number of bridges is transferred into loops under shear, but only at high strain rates. The change in number of links occurs almost instantaneously and corresponds with the overshoot in the stress response. This indicates that the connectivity of the network and the nature of the links (weight) needs to be taken into account to explain the stress drop, and not merely the number of bridging chains in the system. The observed rearrangement is a direct consequence of shear-induced aggregation.

Chapter 6

Percolation and gelation

We discuss the percolation properties of a polymeric gel network. Because of its reversible nature, geometric percolation occurs at a temperature well above the gel transition. To understand rheological changes that take place at the transition, the network consisting of long-lived junctions needs to be taken into account. For this network, a percolating path ceases to exist after a certain time that depends on temperature. We show that Vogel-Fulcher-Tamman (VFT) theory describes this temperature-dependence with high accuracy and that the temperature at which this time diverges corresponds to $T_0 = 0.29$. This is in perfect agreement with the gelation temperature obtained from earlier work. Next, we study the temperature-dependence of the percolation properties. A master curve can be constructed for the percolation probabilities and survival rates. The empirical scaling factors follow the Williams-Landel-Ferry (WLF) equation. The T_0 obtained from WLF is in exact agreement with the one obtained from VFT. These results are important in support of recent discussions that report on similarities between gelation phenomena and glass transition.

63

6.1 Introduction

Percolation theory describes the transition between a state where the system consists of a set of finite size aggregates to a state where an infinite cluster spans the system. In previous work, we showed that in glassy systems, percolation is strongly related to the glass transition [62]. For a thin glassy film confined between two walls, heterogeneity in the dynamics was found. This heterogeneity peaks at a specific time interval. When the mobility is considered over this time interval, throughout the system domains of clearly lower mobility exist. Percolation in the direction perpendicular to the wall of such immobile beads occurs at the glass transition. This causes changes in mechanical properties at this transition.

Also for the gel transition, rheological changes (gelation) are believed to be related to structural changes (percolation). In the classical picture, starting from the sol state, an increase in the volume fraction of the particles (or a decrease in temperature) leads to the formation of aggregates. Eventually, one or more clusters of aggregates will span the system (geometric percolation). These spanning clusters are able to transmit stresses between the opposite sides of the system. As the volume fraction increases further, more and more particles join the spanning cluster and the elastic behavior of the system builds up. However, this picture is only valid for chemical gels, where the junctions are permanent (e.g vulcanized rubber). For the reversible gels in this study, this simplified picture does not hold. In our system, geometric percolation occurs at $T = 1.5$, well above the transition temperatures that are characteristic for a gel transition [19]. At this temperature the system can still flow, since the junctions that give rise to a percolating path only are temporary. Geometric percolation does not take into account the dynamic nature of the gel. Other work already showed that gelation in a system with reversible junctions does not correspond to geometric

percolation [5]. A better approach is to consider only the network formed by the junctions that exist over longer time periods. Therefore in this chapter the goal is to study percolation of the network made up by endgroups who have long-lived junctions and see how this is related to the gel transition.

6.1.1 Relation gel transition and glass transition

Recently it has been pointed out that there are natural parallels between reversible gelation and glass transition [63] and there is considerable interest in unifying these two classes of disordered materials [64]. The glass transition is a reversible transition in amporphous materials from a hard and relatively brittle state into a molten or rubber-like state. There is a massive change in physical properties, such as an increase in relaxation times of many decades. One similarity between glasses and gels lies in relaxation dynamics. For glasses, two pronounced relaxation processes, known as α and β relaxation, govern the near-glass transition. The fast α relaxation originates from the localized motion of particles inside cages that are formed by their neighboring particles. The slow β relaxation expresses the breakup of particle cages. Experimental measurements on the light scattering properties of gelatin indicate analogies to such glass-like relaxation behavior [65]. The long-time component of the relaxation time spectrum follows a power law in relaxation time for both. However the powerlaw exponent has a different sign [66, 67]. Another similarity is that the diffusivity data for the gel can be fit well using the Vogel-Fulcher form, which is known to describe the relaxation in glasses [19]. Furthermore, gels and glasses are difficult to distinguish rheologically. Both show a critical slow down in the approach of the liquid-to-solid transition. Similarities between vitrification and gelation have also been pointed out. Vitrification is the creation of a glass and is achieved by rapidly cooling a liquid through the glass transition. This is similar to the change in dynamic properties that

occur in a gel. At the micelle transition temperature T_m there is an abrupt increase in the number and lifetime of junctions, resulting in the formation of larger, permanent aggregates. Recent work uses a simple lattice model to show that depending on the volume fraction and quench path, the system can behave as a uniform liquid, solution, or as an inhomogeneous glass or gel [68]. It is proposed that a mechanism for gelation is an extension of the glassy state; gelation is seen as an incomplete phase separation arrested by the onset of the glass transition. Also for colloidal gels similarities with gels have been discussed [69]. In the light of these discussions, one of our concerns is to investigate the connection between gelation and glass by studying the temperature dependence of the percolation properties. We show that techniques used for shifting visco-elastic properties in glasses, like Williams-Landel-Ferry and Vogel-Fulcher-Tamman theory, also hold for the gel.

6.2 Survival rate and percolation: Definitions

To study the network consisting of junctions that live longer than average, we introduce the concept of the survival rate. This is defined as the number of junctions between endgroups that have not permanently disappeared after a certain time. This concept is explained in figure 6.1. The numbers on the picture correspond to the sizes of the aggregates that result from the junctions between endgroups. At a certain time t_0 we record the number of junctions n_0 that exist in the system. Then at time interval t= $t_0 + \Delta t$ it is recorded how many of the initial junctions $n(t)$ still exist. The ratio

$$s(t) = n(t)/n_0 \tag{6.1}$$

is called the survival rate (SR). If a junction temporarily breaks in between t_0 and $t_0 + \Delta t$ but forms again later, it is counted as surviving, under the condition it exists

Figure 6.1: Clarification of survival rate. 15 endgroups are shown, with 10 junctions in between them resulting in 4 aggregates. At t_0 there is a path that spans the whole system. At $t_0 + \Delta t$, 3 out of 10 junctions have disappeared. The surviving junctions now form 7 smaller aggregates and percolation has vanished.

at $t_0 + \Delta t$. This fully takes into account the reversible nature of our network. In the example cartoon $n_0 = 10$, $n(t) = 7$ and the SR is 0.7. The junctions in green will not exist anymore at $t_0 + \Delta t$. The time where SR reaches $1/e$ of its initial value is a measure for the effective lifetime [60, 61], as mentioned in the previous chapter. This is measured in rheological experiments, and can be thought of as the average time for the initially bonded junction to no longer recombine.

The system is said to be percolating after a certain time, if the aggregates that result from the surviving junctions between endgroups form a path that spans over the system from the bottom wall to the top wall. In the cartoon the system is initially percolating at t_0. At $t_0 + \Delta t$ some vital junctions are broken and percolation is lost.

6.3 Williams-Landel-Ferry equation

We are interested in describing the effect of temperature on the percolation properties. For glassy systems, above the glass transition there are tremendous changes in viscoelastic properties that characterize the system. Below the glass transition such changes do not appear. The properties can be expressed in terms of a single function at a reference temperature T_{ref}, whose form can be determined experimentally, whether or not it can be conveniently represented by an analytical expression. This is known as the time-temperature superposition and is only valid if the shape of the property is the same for adjacent T. The scaling factors $a(T)$ are determined empirically by making everything superpose:

$$a(T) = \frac{t_T}{t_{T_{ref}}} \tag{6.2}$$

with $t_{T_{ref}}$ and t_T the time for the property of interest to reach a certain level at the reference temperature and the current T. These empirical scaling factors follow the Williams-Landel-Ferry (WLF) equation:

$$\ln a(T) = \frac{-C_1(T - T_{ref})}{C_2 + (T - T_{ref})} \tag{6.3}$$

with C_1 and C_2 empirical constants adjusted to fit the values of $a(T)$. For glassy systems the universal values are $C_1 = 17.44$ and $C_2 = 51.6$ K. WLF is mathematically equivalent to the Vogel-Fulcher-Tamman (VFT) law that is often used to describe the dependence of relaxation times τ on temperature:

$$\tau(T) = \tau_0 \exp(\frac{B}{T - T_0}). \tag{6.4}$$

Here τ_0 and B are material parameters. In previous work studies showed that the relaxation times diverges at $T_0 = 0.29$. This corresponds to the the gelation temperature at which the diffusivity goes to zero, and the viscosity becomes infinite [19]. T_{ref}
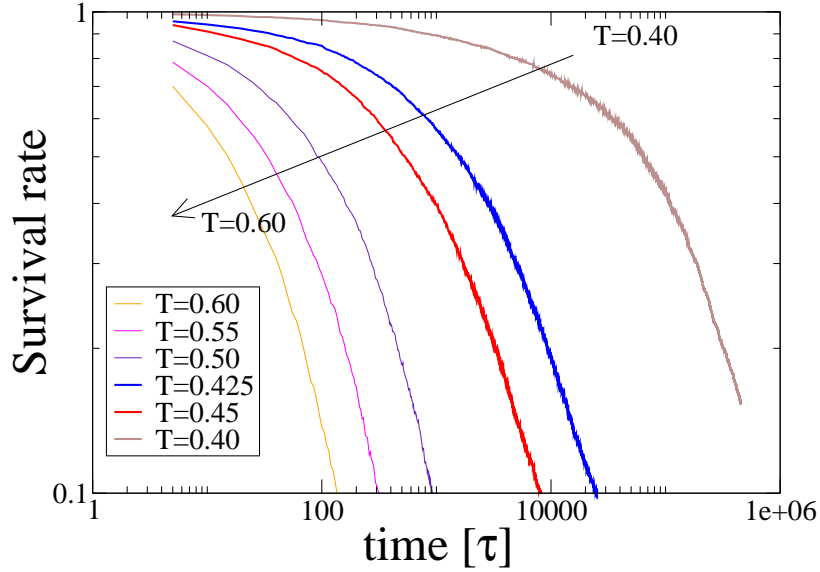
Figure 6.2: The survival rate for different temperatures. Results were obtained by averaging over 5 configurations.

and T_0 are directly related [70]:

$$T_0 = T_{ref} - C_2 \tag{6.5}$$

WLF is typically used in glasses [71]. We are interested to see if the above described techniques hold for the percolation properties of the gel.

6.4 Results

6.4.1 Survival rate and percolation probability

The SR is shown in figure 6.2 on a log-log scale for temperatures between $T = 0.40$ and $T = 0.6$. Results are obtained by averaging over 5 different starting points. For the lower temperatures, the junctions survive over longer times. For $T < 0.4$, the time to simulate the data exceeds practical hardware limits. We introduce the percolation probability. For a time interval Δt we record the surviving junctions for 50 sets, with different starting points. For each set it is checked if at least one percolating path
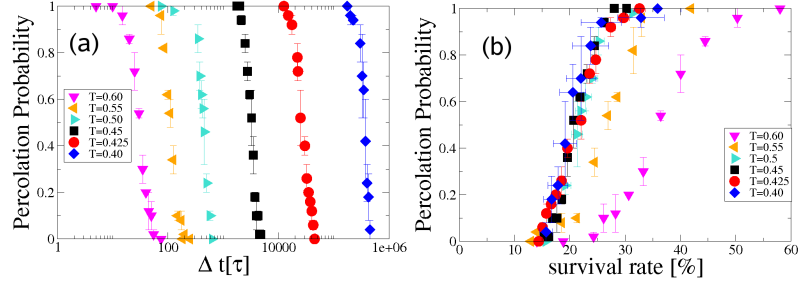
Figure 6.3: (a) Percolation probability as a function of time interval. (b) Same data shifted using emperical scaling factors.

exists that spans across the system, as discussed in figure 6.1. The average probability for this to occur is the percolation probability (PP) and is shown in figure 6.3 (a) as a function of the chosen time interval. The curves display similar shapes, and for the lower temperatures, percolation occurs at much longer time scales. Each time interval results in a corresponding SR. The PP is shown as a function of the SR in figure 6.3 (b). For $T \leq 0.5$ the graphs overlap. The onset of deviations corresponds to the micelle transition temperature $T_m = 0.5$. In previous work it was shown that at this temperature, the number of junctions increases sharply and size distributions become single peaked [19]. It can be understood that these low T show similar percolation behavior, as we showed in chapter 3 that their topology is similar (consisting of a densely connected network of superpeers).

6.4.2 Determination of gelation temperature and T-dependence of percolation properties

The percolation threshold of the system is defined as the time interval for which the PP equals 0.5. This is shown for different temperatures in figure 6.4. When we fit this with VFT, equation (6.4), we obtain $\tau_0 = 0.28$, $B = 1.48$, and a divergence temperature in exact agreement with the gelation temperature found in previous work
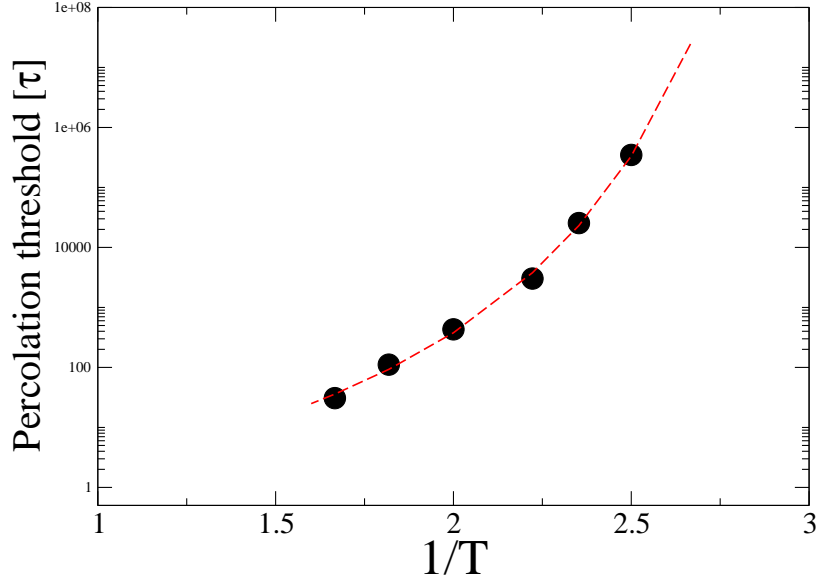
Figure 6.4: Percolation threshold for different temperatures. The VFT fit from equation (6.4) uses $\tau_0 = 0.28054$, $B = 1.48605$, and $T_0 = 0.29375$.

$T_0 = 0.29$. T_0 is independent of the definition of percolation threshold, as the same T_0 is obtained for e.g. a PP of 0.8. This shows that percolation can be used to determine the gelation temperature.

Next, we are interested in seeing if percolation properties show a universal temperature-dependent behavior. We choose $T_{ref} = 0.4$. The motivation for this choice is that the SR still decays significantly so it is computationally possible to gather sufficient data, and it is close to, but above gelation. Figure 6.5 shows the same data as figure 6.3 (a) but shifted empirically so that the curves correspond at $T = 0.4$ for PP 0.5. The used shift factors $a(T)_{PP,emp}$ are shown in table 6.1 and the PPs correspond very well. For $T > 0.6$ the curves clearly differed (not shown here). The corresponding regime is in agreement with the temperature regime up to where the VFT holds in figure 6.4. The WLF constants can now be extracted by fitting $-1/\ln a(T)_{PP,emp}$ using a linearized form of the WLF equation (6.3) [72]. The agreement for this was excellent, with a

correlation coefficient 0.997. We obtain $C_1 = 14.35$ and $C_2 = 0.11$. C_1 is close to the one found for glassy system. C_2 is significantly lower than what is found for glasses, since in our system temperature is expressed in Lennard-Jones units. Table 6.1 also shows that the shift factors $a(T)_{PP,WLF}$, predicted by the WLF equation (6.3), are close to the empirical ones. As the VFT equation is mathematically equivalent to the WLF equation, we should also be able to shift the percolation probabilities using equation (6.4) and the VFT parameters obtained by fitting the percolation tresholds using VFT (figure 6.4). The resulting shift factors $a(T)_{PP,VFT}$ indeed agree with the empirical and WLF shift factors. A final test to see if WLF and VFT hold for the PP is to obtain T_0 using the relation between the WLF and VFT parameters from equation (6.5). We find $T_0 = 0.291$, in agreement with the T_0 from the actual VFT fit in figure 6.4.

Also for the SR a master curve can be obtained using WLF. The shifted curves use empirical shift factors $a(T)_{SR,emp}$ and correspond at SR of 0.5, as shown in figure 6.5 (b). The linearized WLF fit for $a(T)_{SR,emp}$ shows a correlation coefficient 0.986 and we obtain $C_1 = 9.30$ and $C_2 = 0.040$. The table shows that $a(T)_{SR,emp}$ and $a(T)_{SR,WLF}$ correspond closely. The shift factors for SR are different from the ones used for PP. The WLF is typically used for viscoelastic properties such as storage shear modulus, loss modulus, and relaxation modulus. It can be argued that the governing processes in PP are similar to those for relaxation times. This is confirmed by the fact that we found that T_0 from the VFT fit for percolation threshold is the same as the fit obtained from relaxation times.
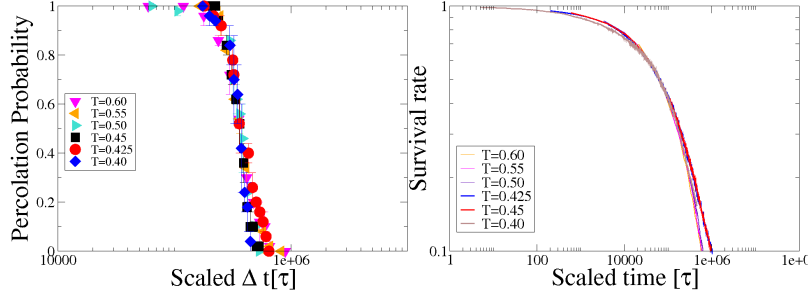
Figure 6.5: (a) Percolation probability from figure 6.3 (a) shifted empirically. (b) Survival rate from figure 6.1 shifted empirically. In both cases $T_{ref} = 0.4$. The scaling factors $a(T)_{pp,emp}$ and $a(T)_{sr,emp}$ are shown in table 6.1.

Table 6.1: Shift factors for percolation probabilities (PP) and survival rates (SR) for $T_{ref} = 0.40$. The scaling factors are obtained as follows: $a(T)_{PP,emp}$ through equation (6.2) with t_T the time at which PP is 0.5; $a(T)_{PP,WLF}$ using equation (6.3) with $C_1 = 14.35$ and $C_2 = 0.11$; $a(T)_{PP,VFT}$ using equation (6.4) with $\tau_0 = 0.28054$, $B = 1.48605$, and $T_0 = 0.29375$; $a(T)_{SR,emp}$ with t_T the time at which SR 0.5; $a(T)_{SR,pred}$ through equation (6.3) with $C_1 = 9.30$ and $C_2 = 0.040$.

T	$\ln a(T)_{PP,emp}$	$\ln a(T)_{PP,WLF}$	$\ln a(T)_{PP,VFT}$	$\ln a(T)_{SR,emp}$	$\ln a(T)_{SR,WLF}$
0.40	0	0	0	0	0
0.425	-2.67	-2.69	-2.66	-3.71	-3.62
0.45	-4.72	-4.53	-4.48	-4.79	-5.21
0.50	-6.75	-6.89	-6.78	-6.53	-6.68
0.55	-8.1	-8.33	-8.19	-7.55	-7.37
0.60	-9.39	-9.31	-9.13	-8.35	-7.77

6.5 Conclusions

In summary, we show that the percolation properties of the network made up of junctions that survive over longer timescales can be used to determine the gelation temperature. The percolation threshold at a certain temperature is a measure for the time at which percolation ceases to exist in the surviving network. These thresholds follow VFT behavior and it is predicted that at $T_0 = 0.29$ this timescale diverges. This is in agreement with the gelation temperature obtained in earlier work and

shows that percolation can be used to obtain the gelation point. Next we studied the temperature dependence of the percolation probabilities. These show universal behavior and a master curve can be constructed. The empirical scaling factors follow the WLF equation, which is commonly used to describe the connection between the temperature and the relaxation time of a polymeric material. Also the survival rates correspond when shifted using WLF. The idea that VFT and WLF hold in our system is further confirmed by the fact that the T_0 from WLF is in agreement with the one we obtained from the VFT fit of the percolation thresholds. Our results support the idea that the gel transition shows similarities to the glass transition. It is important to further quantify this agreement. Molecular glasses show specific aging signatures, such as intrinsic isotherms, asymmetry of approach, and memory effect. To elucidate the relationship between the behavior of colloidal suspension and glasses, these signatures have been tested in recent work [73]. Similar tests could be performed for reversible gels.

Chapter 7

General conclusions and future prospects

In this dissertation we have performed a detailed study of a simulated telechelic polymer gel network. In chapter 3 we focus on the network when there is no stress applied. Concepts from complex network theory were used, by identifying the aggregates as nodes and the polymer chains as links. The degree distribution is bimodal and consists of two Poissonians. We distinguish between two different communities of nodes; peers and superpeers. The average degrees of both Poissonians and the ratio of peers to superpeers changes and depends on the temperature. By creating dummy networks that show matching eigenvalue properties to the simulated gel, we characterize the topological changes that accompany the sol-gel transition temperatures. Below the micelle transition temperature, the network takes a resilient structure. It consists of a highly connected network of superpeers, of which some are connected to "dangling" peers, while the peers do not show connections amongst themselves. Such a bimodal network is very robust against failure and is common in design of informatics networks.

As a continuation of this work, the chemical kinetics of the aggregation processes were recently studied in our group [74]. Aggregates can either break apart producing

smaller components or join together forming larger size aggregates. This can give more information on how the larger aggregates in the system are formed- does this take place by joining two medium-sized aggregates or does it occur progressively by adding single endgroups? From this study it seems that at low temperatures (T=0.45) aggregates mainly form by addition of smaller size aggregates to an existing larger one. The breaking process is different- aggregates break into more or less equally sized aggregates. At higher temperatures the reactions are more uniform: aggregates break into aggregates of all different sizes.

While studying the eigenvalue spectra of the gel, it was observed that spatial dependent networks show asymmetric eigenvalue spectra. By introducing a spatial dependence to ER, spatial, and small-world networks, it is shown in chapter 4 that a positively skewed spectrum is a universal property for all spatial dependent networks. Eigenvalue spectrum can be used to measure the clustering of a network (figure 4.5) and the relation between clustering coefficient and skewness of the network is mathematically derived in equation (4.17). Because of the ongoing developments in geographical information systems (GIS), spatial data is collected on many real-world systems. It would be interesting to calculate eigenvalue spectra for such networks and match our findings with real-world examples. The spectra gives more information than traditional tools to measure clustering, such as Euclidean distance or path lengths, and could be included in GIS mapping software.

Eventually the goal is to study our system under stress, as many of the applications of gels deal with out of equilibrium systems. In chapter 5 we studied the system under application of a constant shear rate. The transient stress response shows viscoelastic properties: a stress overshoot, followed by a stress drop and fluctuations around an average value. There is a region in which the average stress does not significantly increase when the shear rate is increased over several orders of magnitudes.

Within this region, the velocity profiles shows signs of shear-banding and the system consists of two bands that move with a different shear rate. The interface between those bands shows spatiotemporal fluctuations. The lever rule, that predicts a smooth interface between the bands whose position moves with increasing shear rate, does not hold in our system. The simulation allows for a detailed study of possible differences between physical properties between both bands. This gives us new information on atomic concentration, lifetime of junctions, average aggregate size and size distributions in both bands, which are experimentally impossible to measure. We find that some of these properties change gradually across the polymer film, but no sharp increase is detected at the interface. The system shows shear-induced aggregation, and larger aggregates are formed upon application of shear. These aggregates are connected by links of higher weight, while weak links of low weights, break more easily. The resulting size distribution is bimodal, once again indicating a restructuring of the system. We observe a decrease in number of bridging chains in favor of the number of loops, but only at timescales far longer than at which the initial rearrangement occurs. Future work should consist of studying the exact structural changes in more depth. A time-dependent picture of the changing topology is of interest. Also a study of the reaction rates under shear is important. This, in combination with a study of the reaction rates of the loops and bridges might reveal more information on how the rearranged structure comes into existence and what changes occur after the initial rearrangement.

Our current experiments are performed under constant shear. Oscillatory shear measurements can be a source of new information. In such experiments the top wall is oscillated by applying a sinusoidal strain. In small oscillatory shear measurements (SAOS) the response is linear. For large oscillatory shear measurements (LAOS), the deformations are larger and the system shows non-linear behavior. From the stress

response the dynamic moduli can be calculated. The in-phase behavior (storage or elastic modulus) G' measures the stored energy and represents the elastic portion. The out-of-phase behavior (loss or viscous modulus) G'' represents the energy dissipated as heat, the viscous portion. The moduli can also be studied as function of temperature. In this way the dynamical gelation point, the cross-over point between G' and G'' as a function of temperature, can be determined. Also, gels have a uniform and predictable rheological response in vivo, regardless of the mechanical environment to which they are subjected. It can be tested if G' does not change significantly for different ranges of the stress and strain, as is the case for triblock copolymers [14].

The relation between percolation and gelation has been a topic of discussion over several decades. In chapter 6 the approach for this problem is to only look at the part of the gel network that survives over long timescales. This network is responsible for the rheological behavior that makes gels so interesting. The percolation threshold is a measure for the timescale at which a percolating path in this network ceases to exist. The change with temperature of this timescale can be described by the Vogel-Fulcher-Tamman law. We show that at the gelation temperature, the percolation threshold diverges. This indicates percolation can be used to determine the glass transition. Next, it is shown that a master curve can be constructed by shifting percolation properties such as percolation probability and survival rate. The shift factors are well described by the Williams-Landel-Ferry equation. As this is a method commonly used for shifting viscoelastic properties in glasses, this is in support of recent discussions that point out similarities between glass and gel transition. The three classical aging signatures observed in molecular glasses could be tested to give more insight in these similarties. In such experiments, structural properties are measured after performing specific temperature changes. For instance, one could measure the time for the property to reach equilibrium, upon cooling to an increasingly lower

temperature. Another experiment consists of two temperature change steps with the same magnitude: a down-jump from $T_1 + \Delta$ to T_1 and an up-jump from $T_1 - \Delta$ to T_1, and a measurement of the recovery in both cases. Also memory experiments can be performed, in which the sample is first cooled from T_0 to T_i, allowed to partially recover, and then again increased. Similar aging experiments could be performed to further quantify similarities between gels and glasses.

Curriculum Vitae

Joris Billen

Born in Herk-de-Stad, Belgium, August 10, 1982

Education

PhD in Computational Science.	***April 2012***	Claremont Graudate University, Claremont, CA & San Diego State University, San Diego, CA
	PhD thesis: "Simulated associating polymer networks" Advisor: A. Baljon GPA: 3.82	
IWT fellow	***August 2007***	IMEC, Leuven, Belgium
	Topic: "Organic non-volatile memories" Advisor: P. Heremans	
Master of Science in Applied Physics	***August 2005***	Eindhoven University of Technology, Eindhoven, The Netherlands
	M.Sc. thesis at Philips Research: "Blue Polymer LEDs: experiments and modeling" Advisor: R. Coehoorn	
Bachelor of Science in Physics	***July 2002***	Universiteit Hasselt, Belgium
	graduated with distinction	

Publications

1. S.L.M. VAN MENSFOORT, <u>J. BILLEN</u>, S. I. E. VULTO, R. A. J. JANSSEN, AND R. COEHOORN 2011 Predictive modeling of the current density and radiative recombination in blue polymer-based light-emitting diodes *J. Appl. Phys.* **109**, 064502.

2. <u>JORIS BILLEN</u>, MARK WILSON, ARLETTE BALJON, AVINOAM RABINOVITCH 2009 Eigenvalue spectra of spatial dependent networks *Phys. Rev. E.* **80**, 046116.

3. <u>J. BILLEN</u>, M. WILSON, A. RABINOVITCH, AND A. R. C. BALJON 2009 Topological changes at the gel transition of a reversible polymeric network *Eur. Phys. Lett.* **87**, 68003.

4. S. L. M. VAN MENSFOORT, <u>J. BILLEN</u>, S. I. E. VULTO, R. A. J. JANSSEN, AND R. COEHOORN 2009 Electron transport in polyfluorene-based sandwich-type devices: Quantitative analysis of the effects of disorder and electron traps *Phys. Rev. B.* **80**, 033202.

5. R. MÜLLER, <u>JORIS BILLEN</u>, AARON KATZENMEYER, LUDOVIC GOUX, DIRK J. WOUTERS, JAN GENOE AND PAUL HEREMANS 2008 Resistive Electrical Switching of Cu+ and Ag+ based Metal-Organic Charge Transfer Complexes *Mater. Res. Soc. Proc.* **1071**, F06.04.

6. R. MÜLLER, <u>JORIS BILLEN</u>, AARON KATZENMEYER, LUDOVIC GOUX, DIRK J. WOUTERS, JAN GENOE AND PAUL HEREMANS 2007 Electrical Properties of CuTCNQ Based Organic Memories Targeting Integration in the CMOS Back End-of-line *Mater. Res. Soc. Proc.* **997**, I01-10.

7. <u>J. BILLEN</u>, S. STEUDEL, R. MÜLLER, J. GENOE, AND P. HEREMANS 2007 A comprehensive model for bipolar electrical switching of CuTCNQ memories *Appl. Phys. Lett.* **91**, 263507.

8. R. MÜLLER, R. NAULAERTS, <u>J. BILLEN</u>, J. GENOE, AND P. HEREMANS 2007 CuTCNQ resistive nonvolatile memories with a noble metal bottom electrode *Appl. Phys. Lett.* **90**, 063503.

9. R. COEHOORN, S. VULTO, S.L.M. VAN MENSFOORT, <u>J. BILLEN</u>, M. BARTYZEL, H. GREINER, AND R. ASSENT 2006 Measurement and modeling of carrier transport and exciton formation in blue polymer light emitting diodes *Proc. SPIE* **6192**, 619200.

10. ARLETTE R. C. BALJON, <u>JORIS BILLEN</u>, AND RAJESH KHARE
2004 Percolation of Immobile Domains in Supercooled Thin Polymeric
Films *Phys. Rev. Lett.* **93**, 255701.

Conferences (only oral presentations)

	October The Society of Rheology 83nd Annual ***2011*** Meeting
SOR 2011, *Cleveland, OH*	1. <u>J. BILLEN</u>, AND A. R. C. BALJON Microscopic differences between shear bands obtained from simulations of associating polymers 2. A. R. C. BALJON, <u>J. BILLEN</u>, AND A. COLEMAN, AND R. KHARE Dynamic arrest and creep in a simulated associative polymer gel
	October The Society of Rheology 82nd Annual ***2010*** Meeting
SOR 2010, *Santa Fe, NM*	3. <u>J. BILLEN</u>, J. STEGEN, AND A.R.C. BALJON A computational study of shear banding in reversible associating polymers
	March American Physical Society March ***2010*** Meeting 2010
APS 2010, *Portland, OR*	4. <u>J. BILLEN</u>, J. STEGEN, M. WILSON, A. RABINOVITCH AND A. R. C. BALJON Shear banding in a simulated telechelic polymeric gel
	March American Physical Society March ***2009*** Meeting 2009
APS 2009, *Pittsburgh, PA*	5. <u>J. BILLEN</u>, M. WILSON, A. RABINOVITCH AND A. R. C. BALJON Influence of spatial dependence on the eigenvalue spectrum of complex networks
	March Materials Research Society 2008 ***2008***
MRS 2008, *San Francisco,* *CA*	6. R. MÜLLER, <u>JORIS BILLEN</u>, AARON KATZENMEYER, LUDOVIC GOUX, DIRK J. WOUTERS, JAN GENOE, AND PAUL HEREMANS Resistive Electrical Switching of Cu+ and Ag+ based Metal-Organic Charge Transfer Complexes
	September Materials Today Asia ***2007***
Materials Today *2007* *Bejing, China*	7. PAUL HEREMANS, R. MÜLLER, <u>J. BILLEN</u>, A. KATZENMEYER, L. GOUX, D.J. WOUTERS, AND J. GENOE CuTCNQ based nonvolatile organic memories
	May 2007 2nd International Conference on Memory Technology and Design
ICMTD'07, *Giens, France*	8. <u>J. BILLEN</u>, R. MÜLLER, J. GENOE, AND P. HEREMANS Statistical study on the threshold voltage of enhanced cutcnq non-volatile memories

	March 2007 Materials Research Society 2007
MRS 2007, San Francisco, CA	9. R. Müller, <u>J. Billen</u>, R. Naulaerts, O. Rouault, L. Goux, D.J. Wouters, J. Genoe, and P. Heremans Resistive Electrical Switching of Cu+ and Ag+ based Metal-Organic Charge Transfer Complexes
	March 2005 American Physical Society Meeting 2005
MRS 2005, Los Angeles, CA	10. A. Baljon, <u>J. Billen</u>, R. Khare Heterogeneous dynamics in thin films of glassy polymers

Additional information

Scholarships	*2010* Inamori Fellowship Fellowship trhough the Inamori Foundation.
	2005-2006 IWT Fellowship through the Flemish government agency for Innovation by Science and Technology (IWT).
Languages	Dutch - mother tongue English - fluent French - good understanding, reading, and writing Spanish - decent understanding, basic communication

Bibliography

[1] Taisuke Fujimoto, Emi Yoshimoto, and Masahiko Annaka. Study on self-assembly of telechelic hydrophobically modified poly(N-isopropylacrylamide) in water. *Progr. Colloid. Polym. Sci.*, 136:77–86, 2009.

[2] J. Sprakel, E. Spruijt, M. A. Cohen Stuart, N. A. M. Besseling, M. P. Lettinga, and J. van der Gucht. Shear banding and rheochaos in associative polymer networks. *Soft Matter*, 4:1696–1705, 2008.

[3] Sandra Lerouge, Jean-Paul Decruppe, and Jean-Franois Berret. Correlations between rheological and optical properties of a micellar solution under shear banding flow. *Langmuir*, 16(16):6464–6474, 2000.

[4] E. J. Goethals. *Telechelic Polymers: Synthesis and Applications.* CRC Press, Boca Raton, FL, USA, 1989.

[5] S. K. Kumar and J. F. Douglas. Gelation in physically associating polymer solutions. *Phys. Rev. Lett.*, 87(18):188301, 2001.

[6] E. J. Regalado, J. Selb, and F. Candau. Viscoelastic behavior of semidilute solutions of multisticker polymer chains. *Macromolecules*, 32(25):8580, 1999.

[7] Erik Miller and Jonathan P. Rothstein. Transient evolution of shear-banding wormlike micellar solutions. *Journal of Non-Newtonian Fluid Mechanics*, 143(1):22 – 37, 2007.

[8] F. C. MacKintosh, J. Käs, and P. A. Janmey. Elasticity of semiflexible biopolymer networks. *Phys. Rev. Lett.*, 75:4425–4428, 1995.

[9] B. Hinner, M. Tempel, E. Sackmann, K. Kroy, and E. Frey. Entanglement, elasticity, and viscous relaxation of actin solutions. *Phys. Rev. Lett.*, 81:2614–2617, 1998.

[10] Kendra A. Erk, Kevin J. Henderson, and Kenneth R. Shull. Strain stiffening in synthetic and biopolymer networks. *Biomacromolecules*, 11(5):1358–1363, 2010.

[11] Marc W. T. Werten, Helena Teles, Antoine P. H. A. Moers, Emil J. H. Wolbert, Joris Sprakel, Gerrit Eggink, and Frits A. de Wolf. Precision gels from collagen-inspired triblock copolymers. *Biomacromolecules*, 10(5):1106–1113, 2009.

[12] S Amin, S Rajabnezhad, and K. Kohli. Hydrogels as potential drug delivery systems. *Scientific Research and Essay*, 3(11):1175–1183, 2009.

[13] B. Thomas, C. Fryman, K. Liu, and J. Mason. Hydrophilic-hydrophobic hydrogels for cartilage replacement. *J. Mech. Behav. Biomed. Matter*, 2:588, 2009.

[14] Khaled A. Aamer, Heidi Sardinha, Surita R. Bhatia, and Gregory N. Tew Tew. Rheological studies of plla-peo-plla triblock copolymer hydrogels. *Biomaterials*, 25(6):1087 – 1093, 2004.

[15] Jennifer M. Singelyn, Priya Sundaramurthy, Todd D. Johnson, Pamela J. Schup-Magoffin, Diane P. Hu, Denver M. Faulk, Jean Wang, Kristine M. Mayle, Kendra Bartels, Michael Salvatore, Adam M. Kinsey, Anthony N. DeMaria, Nabil Dib, and Karen L. Christman. Catheter-deliverable hydrogel derived from decellularized ventricular extracellular matrix increases endogenous cardiomyocytes and preserves cardiac function post-myocardial infarction. *J Am Coll Cardiol*, 59(8):751–763, 2012.

[16] K. Gawel, D. Barriet, M. Sletmoen, and B. Stokke. Responsive hydrogels for label-free signal transduction within biosensors. *Sensors*, 10:4381–4409, 2010.

[17] J.-F. Berret and Y. Séréro. Evidence of shear-induced fluid fracture in telechelic polymer networks. *Phys. Rev. Lett.*, 87:048303, 2001.

[18] K. Kremer and Gary. S. Grest. Dynamics of entangled linear polymer melts: A molecular-dynamics simulation. *The Journal of Chemical Physics*, 92(8):5057–5086, 1990.

[19] A. R. C Baljon, D. Flynn, and D. Krawzsenek. Numerical study of the gel transition in reversible associating polymers. *The Journal of Chemical Physics*, 126(4):044907, 2007.

[20] G. W. Gear. *Numerical Initial Value Problems in Ordinary Differential Equations*. Prentice-Hall, Englewook Cliffs, NJ, USA, 1971.

[21] J. Billen, M. Wilson, A. Rabinovitch, and A. R. C. Baljon. Topological changes at the gel transition of a reversible polymeric network. *Europhysics Letters*, 87:68003, 2009.

[22] D. Bedrov, G. D. Smith, and J. F. Douglas. Influence of self-assembly on dynamical and viscoelastic properties of telechelic polymer solutions. *Europhys. Lett.*, 59(3):384, 2002.

[23] S. Bocaletti, V. Latora, Y. Moreno, M. Chavez, and D.-U. Hwang. Complex networks: Structure and dynamics. *Phys. Rep.*, 424(4-5):175, 2006.

[24] Y. Bohbot-Raviv, T. M. Snyder, and Z.-G. Wang. Reversible association of telechelic molecules: An application of graph theory. *Langmuir*, 20(18):7860, 2004.

[25] S. K. Kumar and A. Z. Panagiotopoulos. Thermodynamics of reversibly associating polymer solutions. *Phys. Rev. Lett.*, 82(25):5060, 1999.

[26] W. Nejdl, M. Wolpers, W. Siberski, C. Schmitz, M. Schlosser, I. Brunkhorst, and A. Loser. Super-peer-based routing strategies for rdf-based peer-to-peer networks. *Web Semant.*, 1:177, 2003.

[27] J. Davidsen, H. Ebel, and S. Bornholdt. Emergence of a small world from local interactions: Modeling acquaintance networks. *Phys. Rev. Lett.*, 88(12):128701, 2002.

[28] Illés J. Farkas, Imre Derényi, Albert-László Barabási, and Tamás Vicsek. Spectra of "real-world" graphs: Beyond the semicircle law. *Phys. Rev. E*, 64(2):026704, 2001.

[29] T. Tanizawa, G. Paul, R. Cohen, S. Havlin, and H. E. Stanley. Optimization of network robustness to waves of targeted and random attacks. *Phys. Rev. E*, 71(4):047101, 2005.

[30] A. X. C. N. Valente, A. Sarkar, and H. A. Stone. Two-peak and three-peak optimal complex networks. *Phys. Rev. Lett.*, 92(11):118702, 2004.

[31] J. Billen, M. Wilson, A. R. C. Baljon, and A. Rabinovitch. Eigenvalue spectra of spatial-dependent networks. *Phys. Rev. E*, 80(4):046116, 2009.

[32] G. Wang, J.and Provan. Topological analysis of specific spatial complex networks. *Adv. Complex Syst.*, 12(1):45, 2009.

[33] N. Voges, Ad Aertsen, and S. Rotter. Statistical analysis of spatially embedded networks: From grid to random node positions. *Neurocomputing*, 70(10-12):1833 – 1837, 2007. Computational Neuroscience: Trends in Research 2007, Computational Neuroscience 2006.

[34] M. T. Gastner and M. E.J. Newman. The spatial structure of networks. *The European Physical Journal B - Condensed Matter and Complex Systems*, 49:247–252, 2006.

[35] R. Guimer, S. Mossa, A. Turtschi, and L. A. N. Amaral. The worldwide air transportation network: Anomalous centrality, community structure, and cities' global roles. *Proceedings of the National Academy of Sciences of the United States of America*, 102(22):7794–7799, 2005.

[36] Parongama Sen, Subinay Dasgupta, Arnab Chatterjee, P. A. Sreeram, G. Mukherjee, and S. S. Manna. Small-world properties of the indian railway network. *Phys. Rev. E*, 67(3):036106, 2003.

[37] R. Xulvi-Brunet and I. M. Sokolov. Growing networks under geographical constraints. *Phys. Rev. E*, 75(4):046117, 2007.

[38] C. Bauch and D. A. Rand. A moment closure model for sexually transmitted disease transmission through a concurrent partnership network. *Proceedings of the Royal Society of London. Series B: Biological Sciences*, 267(1456):2019–2027, 2000.

[39] Petter Holme and Beom Jun Kim. Growing scale-free networks with tunable clustering. *Phys. Rev. E*, 65(2):026107, 2002.

[40] D. J. Watts and S. H. Strogatz. Collective dynamics of "small-world" networks. *Nature*, 393:440, 1998.

[41] D. Cvetkovic, M. Doob, and H. Sachs. *Spectra of GraphsTheory and Applications, 3rd ed.* Deutscher Verlag der Wissenschaften, Berlin/Academic, New York, 1980.

[42] D. N. Joanes and C. A. Gill. Comparing measures of sample skewness and kurtosis. *Journal of the Royal Statistical Society: Series D (The Statistician)*, 47(1):183–189, 1998.

[43] Jari Saramäki, Mikko Kivelä, Jukka-Pekka Onnela, Kimmo Kaski, and János Kertész. Generalizations of the clustering coefficient to weighted complex networks. *Phys. Rev. E*, 75(2):027105, 2007.

[44] M. Barthalémy. Crossover from scale-free to spatial networks. *Europhys. Lett.*, 63:915, 2003.

[45] David W. Shattuck, Anand A. Joshi, Dimitrios Pantazis, Eric Kan, Rebecca A. Dutton, Elizabeth R. Sowell, Paul M. Thompson, Arthur W. Toga, and Richard M. Leahy. Semi-automated method for delineation of landmarks on models of the cerebral cortex. *Journal of Neuroscience Methods*, 178(2):385 – 392, 2009.

[46] Matthew W. Liberatore, Florian Nettesheim, Paula A. Vasquez, Matthew E. Helgeson, Norman J. Wagner, Eric W. Kaler, L. Pamela Cook, Lionel Porcar, and Y. Thomas Hu. Microstructure and shear rheology of entangled wormlike micelles in solution. *Journal of Rheology*, 53(2):441–458, 2009.

[47] Matthew E. Helgeson, Paula A. Vasquez, Eric W. Kaler, and Norman J. Wagner. Rheology and spatially resolved structure of cetyltrimethylammonium bromide wormlike micelles through the shear banding transition. *J. Rheol.*, 53(3):727–756, 2009.

[48] Matthew E. Helgeson, Matthew D. Reichert, Y. Thomas Hu, and Norman J. Wagner. Relating shear banding, structure, and phase behavior in wormlike micellar solutions. *Soft Matter*, 5:3858–3869, 2009.

[49] M. R. Lopez-Gonzalez, W. M. Holmes, and P. T. Callaghan. Rheo-nmr phenomena of wormlike micelles. *Soft Matter*, 2:855–869, 2006.

[50] M. A. Fardin, B. Lasne, O. Cardoso, G. Grégoire, M. Argentina, J. P. Decruppe, and S. Lerouge. Taylor-like vortices in shear-banding flow of giant micelles. *Phys. Rev. Lett.*, 103:028302, 2009.

[51] Jean-Baptiste Salmon, Annie Colin, Sébastien Manneville, and Fran çois Molino. Velocity profiles in shear-banding wormlike micelles. *Phys. Rev. Lett.*, 90:228303, Jun 2003.

[52] S. Lerouge, M. Argentina, and J. P. Decruppe. Interface instability in shear-banding flow. *Phys. Rev. Lett.*, 96(8):088301, 2006.

[53] Suzanne M. Fielding. Complex dynamics of shear banded flows. *Soft Matter*, 3:1262–1279, 2007.

[54] M.W. Johnson Jr. and D. Segalman. A model for viscoelastic fluid behavior which allows non-affine deformation. *Journal of Non-Newtonian Fluid Mechanics*, 2(3):255 – 270, 1977.

[55] S. M. Fielding. Linear instability of planar shear banded flow. *Phys. Rev. Lett.*, 95:134501, 2005.

[56] Sébastien Manneville, Annie Colin, Gilles Waton, and Fran çois Schosseler. Wall slip, shear banding, and instability in the flow of a triblock copolymer micellar solution. *Phys. Rev. E*, 75:061502, 2007.

[57] Joris Sprakel, Evan Spruijt, Martien A. Cohen Stuart, Matthias A. J. Michels, and Jasper van der Gucht. Intermittent dynamics in transient polymer networks under shear: Signs of self-organized criticality. *Phys. Rev. E*, 79(5):056306, 2009.

[58] P. G. Khalatur, A. R. Khokhlov, and D. A. Mologin. Simulation of self-associating polymer systems. i. shear-induced structural changes. *J. Chem. Phys.*, 109(21):9602–9613, 1998.

[59] Tsuyoshi Koga, Fumihiko Tanaka, Isamu Kaneda, and Franoise M. Winnik. Stress buildup under start-up shear flows in self-assembled transient networks of telechelic associating polymers. *Langmuir*, 25(15):8626–8638, 2009.

[60] Robert S. Hoy and Glenn H. Fredrickson. Thermoreversible associating polymer networks. i. interplay of thermodynamics, chemical kinetics, and polymer physics. *The Journal of Chemical Physics*, 131(22):224902, 2009.

[61] Alexander N. Semenov and Michael Rubinstein. Thermoreversible gelation in solutions of associative polymers. 1. statics. *Macromolecules*, 31(4):1373–1385, 1998.

[62] Arlette R. C. Baljon, Joris Billen, and Rajesh Khare. Percolation of immobile domains in supercooled thin polymeric films. *Phys. Rev. Lett.*, 93:255701, 2004.

[63] C. Z. Zhang. *Interplay between long-range and short-range interactions in polymer self-assembly and cell adhesion.* PhD thesis, California Institute of Technology, 2007.

[64] Sciortino F. Disordered materials: One liquid, two glasses. *Nat. Mater.*, 1:145, 2002.

[65] S. Z. Ren and C. M. Sorensen. Relaxations in gels: Analogies to α and β relaxations in glasses. *Phys. Rev. Lett.*, 70:1727–1730, 1993.

[66] Francois Chambon and H. Henning Winter. Linear viscoelasticity at the gel point of a crosslinking pdms with imbalanced stoichiometry. *Journal of Rheology*, 31(8):683–697, 1987.

[67] H. Winter, Miriam Siebenbrger, David Hajnal, Oliver Henrich, Matthias Fuchs, and Matthias Ballauff. An empirical constitutive law for concentrated colloidal suspensions in the approach of the glass transition. *Rheologica Acta*, 48:747–753, 2009.

[68] Jennifer E. Witman and Zhen-Gang Wang. A lattice model of vitrification and gelation. *The Journal of Physical Chemistry B*, 110(12):6312–6324, 2006.

[69] Antonio M. Puertas, Matthias Fuchs, and Michael E. Cates. Comparative simulation study of colloidal gels and glasses. *Phys. Rev. Lett.*, 88:098301, 2002.

[70] Chen-Yang Liu, Jiasong He, Roland Keunings, and Christian Bailly. New linearized relation for the universal viscositytemperature behavior of polymer melts. *Macromolecules*, 39(25):8867–8869, 2006.

[71] Nipun J. Soni, Po-Han Lin, and Rajesh Khare. Effect of cross-linker length on the thermal and volumetric properties of cross-linked epoxy networks: A molecular simulation study. *Polymer*, 53(4):1015 – 1019, 2012.

[72] J. D. Ferry. *Viscoelastic Properties of Polymers, Third Edition*. John Wiley & Sons, INC, New York, 1980.

[73] Xiaojun Di, K. Z. Win, Gregory B. McKenna, Tetsuharu Narita, Fran çois Lequeux, Srinivasa Rao Pullela, and Zhengdong Cheng. Signatures of structural recovery in colloidal glasses. *Phys. Rev. Lett.*, 106:095701, 2011.

[74] Mark Wilson, Avinoam Rabinovitch, and Arlette R. C. Baljon. Aggregation kinetics of a simulated telechelic polymer. *Phys. Rev. E*, 84:061801, 2011.